International School for Advanced Studies
Trieste

Two Problems in Condensed Matter Theory:

a) Surface Melting
   with Long-Range Potential
b) Impurity-Impurity Interaction
   in The Honeycomb Lattice

Thesis submitted for the degree of
"Magister Philosophiae"

CANDIDATE
Xiaojie Chen

SUPERVISORS
Prof. Erio Tosatti
Dr. Furio Ercolessi

Surface Melting
with Long-Range Potential

Contents

4   Discussions and Outlook   46

Bibliography   48

Introduction

The idea that crystal melting might be a surface-initiated process when the liquid wets its own solid is very old [1,2]. A massive amount of macroscopic and semi-macroscopic evidence for the appearance, just below the triple point temperature T_m, of a quasi-liquid film at the solid-gas interface, particularly of molecular crystals, has been collected by chemical physicists [3]. More recently, with the advent of powerful surface physics tools, the study of this problem has begun at the microscopic level. Several crystal surfaces which melt—i.e., where a growing quasi-liquid layer forms very near but below T_m, have been identified [4,5,6,7]. Other surfaces have also been found, which exhibit what might be called "non-melting", i.e. no quasi-liquid layer appears at all [8], or if it appears, it does not grow as T_m is approached [9].

While these experimental studies are now expanding, and promise to uncover much rich physics, microscopic theory for surface melting is still a outstanding problem. For a microscopic theory, one would need for a start a simple and accurate model, capable of accounting for the bulk phase diagram including solid, liquid and vapor phases, the triple point and the critical point of any true substance. Such a theory has not yet been identified and the very basic building block for a surface melting theory is missing.

Alternatively, a very popular microscopic model is the so-called SOS model of surface roughening [10,11,12], which accounts well for "vertical" disordering phenomena occur at solid-liquid interface [13], as well as at certain solid-vapor interfaces, such as high-index surfaces [14], where steps either exist already at $T = 0$, or are very easy to produce at low

enough temperatures [15,16]. Unfortunately this model does not possess a triple point — the SOS "crystal" has no vapor and never melts — and is of little use very near T_m, where the three phases coexist with equal status. Due mainly to historical reasons and to the lack of any better theory, roughening is often quoted as a theory of surface melting, although this is clearly improper [17].

Computer simulations, most notably molecular dynamics (MD), would seem in principle well suited to study surface melting. Several molecular dynamics simulations have been carried out over the last decade, aimed at finding and understanding surface melting. By far the most popular system chosen has been a collection of particles with Lennard-Jones (LJ) interaction. The classic work is that of Broughton and Woodcock [18], followed up later by Broughton and Gilmer [19]. The disordering of several surface layers below T_m is quite well characterized by these studies.

Nonetheless, the number of disordered or "melted" layers exhibited by these MD simulations is too small to establish unequivocally that a clear equilibrated quasi-liquid film is forming. Quite recently the opinion has been expressed, based on very similar calculations, that the LJ surfaces do not melt, but rather roughen [20]. This is argued on the grounds that the number of surface vacancies is large, and that the crystal periodic modulation of surface density is never small, so that atoms appear to occupy "lattice positions". However, the true problem does not have to do with surface melting or roughening, both of which we believe to occur on a LJ surface (they are not alternative), but rather with expecting too much of present-day MD calculations. In a microcanonical calculation, the temperature fluctuates by a large amount, of order $\frac{T}{\sqrt{N}}$ (conversely in a canonical calculation, the energy fluctuates, and one is not better off). Hence it is intrinsically difficult to approach T_m by less than say, one percent. This is usually insufficiently close to T_m to have a well-developed quasi-liquid layer, even when this wants to form. While one can rather conclude that in its present version MD is just not the right tool to study surface melting, it turns out that MD allows a perfectly good study of the behavior of surfaces which do not

melt [21].

Recently, Tosatti and Trayanov [22] have proposed a mean-field lattice theory, based on minimization of free energy respect to two parameters, namely density ρ_l and crystallinity c_l. They applied the theory to a LJ system, and found that the thickness of the quasi-liquid layer increases asymptotically like $(T_m - T)^{-\frac{1}{3}}$, rather than like $|\ln(T_m - T)|$ as expected, due to the long-range nature of the full LJ potential [23]. It is interesting, in fact, that the apparently irrelevant weak potential tail should have such a dramatic effect on the quasi-liquid layer. For even longer-ranged potentials, such as one expected for molecular species that have a permanent dipole moment, the quasi-liquid layer thickness should be enhanced even more. This, in the end, might be the reason why some of these molecular crystals offer the best examples of macroscopically observable quasi-liquid layers [3]. Before proceeding further with the contents of this thesis, two additional remarks can be made:

- The first is that the liquid film thickness diverges like $t^{-\frac{1}{\nu-d}}$, where $t = \frac{T_m - T}{T_m}$, ν is the interaction tail exponent, $\nu = 6$ for LJ system, and d is the space dimension. This is in fact a general result, already well-known in the theory of wetting [24,25] and will be further discussed in section 1.1.2.

- A second, more important remark concerns the physical explanation of why should long-range forces yield a thicker quasi-liquid film. A qualitative explanation could be that of Tosatti [26], according to which the long-range attractive tail has the effect of shifting the interface between two phases, in favour of the denser one (see section 1.1.1). Since the mean density difference between the liquid phase and the gas phase is much larger than that between the solid and the liquid, we expect the quasi-liquid film thickness to be increased with a longer-range attractive tail.

The idea of the present work is to choose a very long ranged potential, which asymptotically behaves like $r^{-\nu}$, $\nu < 6$. Such a potential is not meant to describe any particular real physical system. But we expect

it (see chapter 1 and Ref. [23]) to give rise to an enhanced "super-premelting" (SM), with many more layers melted than a LJ system ($\nu = 6$) at same value of $t = \frac{T_m - T}{T_m}$. Hence, with this fictitious system, we should be able to clearly observe surface melting by computer simulation. The hope is to be able to equilibrate a thin liquid film of perhaps 5 – 10 layers thickness, at temperature near, but significantly below the bulk melting temperature, and then study carefully for the first time its static and dynamic properties.

The organization of this thesis is the following: in chapter 1, we describe in some detail our model potential, and discuss some effects due to its long range behavior. We present in chapter 2, some of the preliminary results we obtained in a simulation of a bulk solid crystal, based on our model potential. The motivation for this bulk work is two-fold:

- Adjust some system dependent parameters of the MD simulation program [27] (such as time step, etc.);

- Locate the relevant bulk coexistence lines and the solid lattice constants near melting.

These quantities are very important for the surface melting simulation, described in detail in chapter 3. Some interesting results have been obtained, in good agreement with expectations based on mean-field theory (see chapter 1 and ref. [15,23]). Preliminary hints of unexpected features have been found at lower temperatures. If confirmed, they might begin to shed light on very unexplored aspects of surface melting, connected with the first-layer break-up. The results are discussed, with some outlooks, in chapter 4.

Chapter 1

Long-Ranged Potential

1.1 Mean-field theory of melting

We have mentioned in the introduction that the long-range (LR) inter-
action has important effects on the premelting behavior of the crystal.
In particular, the melt growth exponent depends on the interaction tail
in a critical way. While a thorough understanding of the melting phe-
nomena is still an open problem in condensed matter physics, theories
based on mean-field approximations (MFA) have been found to be able
to give the correct growth exponent [29,23,25,22,5,30], as well as the
bulk behavior of the surface free energy.

1.1.1 Phenomenological explanation of melt growth

To give a phenomenological explanation of the melt growth [26], suppose
we have a system of particles interacting by a short-range potential near
the triple point. The lower half space is assumed to be occupied by
particles in the solid phase, while the upper half space by gas particles.
Furthermore, let us suppose the solid to be wetted by a quasi-liquid layer
of a certain thickness l located in between the solid and the vapor. This
occurs when, as it is usually the case, the sum of the solid-liquid and
liquid-vapor interface free energies is lower than the solid-gas interface
free energy [31,30,32,25].

The thickness l is very modest for short-range (SR) forces, obeying the growth law:

$$l \propto |\ln |T - T_0||$$ (1.1)

with T_0 the transition temperature. Turning on the LR attractive tail has the effect, first of all, to shift the solid-gas as well as the liquid-gas and solid-liquid bulk coexistence lines, in favour of the denser phases. That means, for our system, that some liquid will be recrystallized, moving upwards the solid-liquid interface. At the same time, much more gas particles will condense into liquid, so that the liquid-gas interface also moves upwards, but in a much more pronounced way than the solid-liquid interface. As a result, the liquid layer thickness becomes much larger.

Evidently, this reasoning, based on macroscopic concepts, explains only qualitatively why long-range attractive interactions should favour surface melting. A much more detailed quantitative discussion is given below.

1.1.2 Review of mean-field description of surface melting

Though an appropriate melting theory is still absent, it has been argued that surface melting exhibits the same thermal singularity of complete wetting [25,5]. Let us introduce a simple phenomenological mean-field theory of surface melting [23,24] by observing that the interatomic interaction potentials are repulsive at short distances and attractive at large distances. Dividing them up suitably leads to a reference Helmholtz free energy density $f_h(\rho, T)$, which describes the effects of the hard-core repulsive parts of the interactions. Since the long-range interaction suppresses the fluctuations [33], the attractive parts of the interactions can be treated in mean-field approximation. One obtains then the following grand canonical potential Ω for a given number density profile $\rho(\vec{r})$ [34]:

$$\Omega[\{\rho(\vec{r})\}, T, \mu] = \int d\vec{r} f_h[\{\rho(\vec{r})\}, T]$$

6

$$+ \frac{1}{2} \int d\vec{r} \int d\vec{r'} \tilde{w}(|\vec{r} - \vec{r'}|) \rho(\vec{r}) \rho(\vec{r'})$$

$$+ \int d\vec{r}[\rho_w V(\vec{r}) - \mu] \rho(\vec{r}) \tag{1.2}$$

Here, all integrals are taken over the half-space $V_+ = \{\vec{r} = (\vec{r}_\|, z \geq 0)\}$, $\tilde{w}(|\vec{r} - \vec{r'}|)$ is the attractive part of the adsorbate-adsorbate (fluid-fluid) interaction, while the substrate (the semi-infinite solid) potential is $\rho_w V(\vec{r})$, with ρ_w being the mean number density of the substrate. (Note that the number density ρ is the fluid number density.) The substrate-adsorbate interface is assumed to be in the xy plane at $z = 0$. In equation 1.2 the hard core contribution to Ω is treated in a local density approximation. The mean-field solution results from minimizing $\Omega[\{\rho(\vec{r})\}, T, \mu]$ with respect to all density profiles.

One can split this minimization into two steps:

- Minimize $\Omega[\{\rho(\vec{r})\}, T, \mu]$ in that subspace of $\{\rho(\vec{r})\}$ in which all profiles have the same interface position l, so that $\rho(z = \infty)$ equals the gas density $\rho_g(\mu, T)$ in the bulk. The most favourable ones will be those that are liquid-like for $0 < z < l$. In this way one constructs a function $\Omega_s(l; T, \mu)$;

- Minimizing $\Omega_s(l; T, \mu)$ with respect to l yields the mean-field solution $\Omega_s(T, \mu) = \sigma_{g,s}$, and the equilibrium interface position $l(T, \mu)$ within MFA. The actual profile $\rho(\vec{r}; T, \mu)$ corresponds to that profile which minimizes $\Omega[\{\rho(\vec{r})\}, T, \mu]$ in the subspace belonging to $l(T, \mu)$.

An analytic treatment of this approach becomes feasible [25] if so-called square-gradient theories are used. This means that fluid-fluid interaction term in equation 1.2 is expanded into a Taylor series:

$$\frac{1}{2} \int d\vec{r} \int d\vec{r'} \tilde{w}(|\vec{r} - \vec{r'}|) \rho(\vec{r}) \rho(\vec{r'}) =$$

$$-\frac{1}{2} \tilde{w}_0 \int d\vec{r}[\rho(\vec{r})]^2 + \frac{1}{2} \tilde{w}_2 \int d\vec{r}[\vec{\nabla} \rho(\vec{r})]^2 + \bigcirc(\tilde{w}_4) \tag{1.3}$$

with $\tilde{w}_0 = -\int d\vec{r} \tilde{w}(\vec{r}) > 0$, $\tilde{w}_2 = -\frac{1}{6} \int d\vec{r} r^2 \tilde{w}(r)$, and $\tilde{w}_n \sim \int d\vec{r} r^n \tilde{w}(r)$. (The derivation of equation 1.3 uses $\rho(z = 0) = 0$.) A necessary condition for equation 1.3 to be valid is that all the moments $\tilde{w}_n$ exist. This

7

requires that $\tilde{w}(r)$ decays exponentially. For van der Waals forces $\tilde{w}_4$ does not exist (i.e. the integral diverges), so that people in dealing with long-range interactions, approximate the fluid-fluid interaction $\tilde{w}(\vec{r})$ as short-range, and treat the substrate potential as a long-range one. Surprisingly, the thermal singularities obtained are the same, irrespective of whether both interactions or only the substrate potential are long-range [35,36,37].

To proceed, a so-called sharp-kink approximation is employed. In this approximation, the continuous density profile is replaced by piecewise constant functions:

$$\rho(z) = \begin{cases} \rho_l & \text{if } d_w \leq z \leq l \\ \rho_g & \text{if } l < z \leq L \\ 0 & \text{otherwise} \end{cases} \qquad (1.4)$$

Thus, l is the thickness of the liquid layer of density ρ_l, ρ_g is the gas density, d_w is a microscopic distance corresponding to the repulsive hardcore. A macroscopic distance L gives the cutoff of the gas phase.

The effective mean-field potential $\Omega_s(l)$ is the minimum of $\Omega[\{\rho(\vec{r})\}, T, \mu]$ with respect to density profiles $\{\rho(\vec{r})\}$ with a prescribed liquid-gas interface position l. In the sharp-kink approximation, each of these subspaces consists of a single profile, given by equation 1.4. Upon substitution of equation 1.4 into equation 1.2, one finds that the grand canonical potential can be separated into the following bulk (gas) and surface contributions (A denotes the surface area):

$$\Omega[\{\rho(\vec{r})\}, T, \mu] = AL\Omega_b(\rho_g, T, \mu) + A\Omega_s(l, T, \mu) \qquad (1.5)$$

where Ω_b is the bulk term which does not depend on the l, while the surface term Ω_s carries the important l dependence [38,25]:

$$\Omega_s(l) = Stl + \omega(l) + R \qquad (1.6)$$

with $t \equiv (T_m - T)/T_m$, and $S \equiv T_m(S_l - S_c)$, where S_l and S_c are respectively the bulk entropies per unit volume of the liquid and of crystal at T_m, while R represents terms independent on l. The term

8

$\omega(l)$ depends on the interaction forces, and is defined as:

$$\omega(l) = (\rho_l - \rho_g) \left[\rho_l \int_{l-d_w}^{\infty} dy\, t(y) - \rho_w \int_{l}^{\infty} dy\, V(y) \right] \qquad (1.7)$$

where $t(y)$ represents the fluid-fluid interaction potential,

$$
\begin{aligned}
t(y) &= \int_{y}^{\infty} dx\, w(x) \\
w(x) &= \int d^2 r_{\|}\, \tilde{w}((r_{\|}^2 + x^2)^{1/2})
\end{aligned}
\qquad (1.8)
$$

In equation 1.7, $V(y)$ is the substrate potential, it is the three dimensional integral of the long-range interaction potential ϕ:

$$V(z) = \int_{-\infty}^{z} dz' \int d^2 r_{\|}\, \phi(((z - z')^2 + r_{\|}^2)^{1/2}) \qquad (1.9)$$

One can easily prove that for a potential tail of kind:

$$\phi(r) \sim -\frac{a}{r^{\nu}} \qquad (1.10)$$

the leading term in the $V(z)$ is just of

$$V(z) \sim -\frac{u_d}{z^{\sigma}} \qquad (1.11)$$

with u_d constant (the so-called Hamaker constant) and the exponent $\sigma = \nu - 3$.

The mean value $\bar{l}$ of the liquid layer thickness is determined within MFA by:

$$\frac{\partial \Omega_s(l)}{\partial l} = 0 \qquad (1.12)$$

Upon substitution of equations 1.11,1.7,1.6 into equation 1.12, one obtains easily that

$$
\begin{aligned}
\bar{l} &\sim t^{-\eta} \\
\eta &\equiv \alpha_s - 1 = \frac{1}{\sigma}
\end{aligned}
\qquad (1.13)
$$

where α_s is the exponent of the specific heat. For van der Waals forces, one obtains the liquid layer growth exponent $\eta = \frac{1}{3}$, which is in fully agreement with experimental results on Ar [5] and numerical calculations using a Lennard-Jones potential [22].

9

1.2 A model long-ranged potential

Computer simulation studies of surface melting are faced with the problem of the limited temperature (or energy, in a microcanonical simulation) resolution available. Fluctuations are in fact, as large as $1/\sqrt{N}$, or $\sim 1\%$ for a typical system with $N \sim 10000$. On the other hand, the MFA-based study in Ref. [22] reports for example, the presence of a $4 \sim 6$ layers thick quasi-liquid layer only 1% below the melting temperature, for (110) surface of LJ system. This makes the surface melting of the (6-12) LJ system very difficult to investigate by molecular dynamics.

Concerning the choice of our model system in the surface melting studies, on one hand, we would like to have ν as small as possible, so as to obtain a thicker and faster-growing liquid layer. On the other hand, the bulk total energy sum diverges for $\nu \leq 3$, whence a neutralizing background is needed for such potentials. We do not wish to have neutralizing backgrounds in our surface problem, because of the ambiguities it could generate. Therefore, we must have $\nu > 3$.

Also, it should be noted that long-range forces tend to suppress fluctuations. Since we would after all want to observe some fluctuation effects, ν should not be too small. As a compromise between these different motivations, we have chosen $\nu = 4$ for the present study. Precisely, our potential is of the Lennard-Jones type inside a range $r_T = 3.2\sigma$, with σ the hard core distance of the potential, and has a long-ranged tail outside r_T (this form has been used previously by A. Trayanov and E. Tosatti [39]):

$$\phi(r) = \begin{cases} V_{LJ} & \equiv 4\epsilon_0 \left[\left(\frac{\sigma}{r} \right)^{12} - \left(\frac{\sigma}{r} \right)^{6} \right] & \text{if } r \leq r_T; \\ \phi_T(r) & \equiv -\epsilon_0 \frac{a}{(\frac{r}{\sigma}+b)^4} & \text{otherwise.} \end{cases} \quad (1.14)$$

where ϵ_0 is the depth of the Lennard-Jones potential, and a, b are parameters which are determined by the continuities of $\phi(r)$ and $\frac{d\phi(r)}{dr}$ at r_T. With these two conditions, we easily find that $a \simeq 7.738$, and $b \simeq -1.065$.

Clearly, this is an academic system, not particularly related with any "real" system—although the short-range part is rare-gas-like. Its

only purpose is to allow a close examination by computer of the surface melting phenomenon. In fact, according to equation 1.13, we expect this system to have the exponent $\eta = 1$, and therefore to exhibit a surface "super-premelting", which would be clearly observable by MD simulations.

Preliminary results of mean-field based study by Tosatti and Trayanov [39] using the same potential, based on the same technic described in reference [22], confirm this prediction. For a (110) surface, they have obtained the exponent $\eta = 1$. They have observed that the number of molten-layers is about $1 \sim 2$ at 7.5% below T_m, and it rises to about $4 \sim 6$ at 1% below T_m.

In practical numerical calculations, in order to limit the number of interacting pairs, a cutoff range r_c is introduced. The force can be expressed as:

$$\vec{F_i} \equiv \vec{F_1}(\vec{r_i}) + \vec{F_2}(\vec{r_i}) \tag{1.15}$$

where $\vec{F_1}(\vec{r_i})$ represents the force on particle i, due to the surrounding particles within a sphere of radius r_c:

$$\vec{F_1}(\vec{r_i}) = -\sum_{\substack{j=1 \\ j \neq i}}^{N} \vec{\nabla}_i \phi(r_{ij}) \theta(r_c - r_{ij}) \tag{1.16}$$

and $\vec{F_2}(\vec{r_i})$ is the force on particle i due to the particles outside the sphere:

$$\vec{F_2}(\vec{r_i}) = -\sum_{\substack{j=1 \\ j \neq i}}^{N} \vec{\nabla}_i \phi(r_{ij}) \theta(r_{ij} - r_c) \tag{1.17}$$

For convenience, throughout our simulations, we use $r_c = r_T$. In this way, $\vec{F_1}$ is just the force due to interactions by a common (6-12) LJ potential truncated at $r_c = 3.2\sigma$, while $\vec{F_2}$ is the force due to the $\sim 1/r^4$ interaction tail (see Eq. 1.14):

$$\vec{F_2}(\vec{r_i}) = -\sum_{\substack{j=1 \\ j \neq i}}^{N} \vec{\nabla}_i \phi_T(r_{ij}) \theta(r_{ij} - r_c). \tag{1.18}$$

While $\vec{F}_1$ is computed exactly (this amounts to sum explicitly over ~ 140 neighbors), $\vec{F}_2$ is approximated by an analytic method, described in detail in the next chapters.

Chapter 2

Bulk Simulation

2.1 Compensating pressure

In MD calculations of bulk systems, the particles are enclosed in a box (usually a parallelepiped which we also used), and periodic boundary conditions (PBC) are used to minimize the boundary effects. PBC consist of repeating the computational box by rigid translation along the three directions parallel to the box edges, so that the whole space is filled. When computing the forces acting on a given particle i, one then has to include the contributions coming not only from the other particles j in the MD box, but also from their images $j', j'', \cdots$, in the adjacent boxes — if their distance from i is less than the interaction cutoff. Usually however, to reduce greatly the computer time, the cutoff r_c is chosen to be less than $L/2$, where L is the box side length (we assume a cubic box for simplicity). It is easy to show that, with this choice, at most only the nearest of all the images of a particle j can interact with i. For this reason, this construction is called the "nearest image convention". We have adopted it, by using $r_c = 3.2\sigma$ and $L = 7.711\sigma$ (at $T = 0$).

In this way, however, we include only the first term in the force splitting of Eq. 1.15. For the second term which contains the long-range tail contributions, we approximate the system outside a sphere of radius r_c centered on each particle i, with a uniform fluid with density ρ. The tail term is then obtained by integration on this uniform fluid.

13

In a bulk, the tail contribution to the force is zero in this approximation for symmetry reasons. However, the long-range tail has a non negligible effect on the energy. In fact, the tail energy for a particle can be calculated as:

$$V(\vec{r_i}) = 1/2 \sum_{\substack{j=1 \\ (j \neq i)}}^{N} \phi(r_{ij})\theta(r_{ij} - r_c)$$

$$\simeq \pi\rho \int_{-\infty}^{+\infty} dz \int_{0}^{+\infty} \frac{dR^2}{2} \left\{ -\frac{a}{\left[(R^2 + z^2)^{\frac{1}{2}} + b \right]^4} \right\}$$

$$= \alpha\rho \qquad (2.1)$$

with ρ the bulk density, approximated to be constant, and

$$\alpha = \frac{2\pi}{3}(-a) \left\{ \frac{r_c^2}{(r_c + b)^3} + \frac{r_c}{(r_c + b)^2} + \frac{1}{r_c + b} \right\} \qquad (2.2)$$

Here, and from now on, we use the reduced units. For $r_c = 3.2$, $\alpha = -0.36$. This dependence of the energy on the density of the system gives rise to an effective "internal pressure", which we can replace in our bulk simulations with an equivalent external pressure. This pressure, also called "compensating pressure", can be introduced in the following way.

Suppose we have a system with N particles without the tail interactions, in thermodynamic equilibrium (in the absence of pressure) at a certain volume Ω_0. The density is thus $\rho_0 = \frac{N}{\Omega_0}$. At some instant, we turn on the tail forces. After some time, the system will reach a new equilibrium state with volume Ω_1 and density $\rho_1 = \frac{N}{\Omega_1}$. Since the tail contribution E_T to the total energy is proportional to the density,

$$E_T = N\alpha\rho, \qquad (2.3)$$

as the density changes from ρ_0 to ρ_1, the enthalpy will also change by

$$\Delta H = N\alpha\Delta\rho, \qquad (2.4)$$

where

$$\Delta\rho = \rho_1 - \rho_0. \qquad (2.5)$$

14

Analogously, the presence of an external pressure P would also cause a change in volume $\Delta\Omega$, implying an enthalpy change:

$$\Delta H = P\Delta\Omega. \tag{2.6}$$

Of course, for these two interpretations to be equivalent, it's necessary that

$$
\begin{aligned}
P &= N\alpha\frac{\Delta\rho}{\Delta\Omega} \\
&= N\alpha\frac{1}{\Delta\Omega}\Delta\left(\frac{N}{\Omega}\right) \\
&= -\alpha\rho^2. \tag{2.7}
\end{aligned}
$$

Note that, for an attractive tail, $\alpha < 0$, so that P is positive.

Thus, in bulk simulation, by using equation 2.7, we can account for the tail correction by just applying the compensating pressure according to the density of the system. Therefore, as far as bulk properties are considered, our system characterized by potential 1.14 is equivalent to a conventional LJ system under pressure. Of course, this is no longer true when a surface is present.

2.2 Bulk properties

We study a model system composed of particles interacting with one another via the potential described in the previous chapter. For our simulations, we use the constant pressure MD method of Parrinello-Rahman [28], which allows for variations of volume and the shape of the box under the action of the external pressure and the internal stress. The temperature of the system is also kept constant by scaling the particle velocities at each time step. The program we used was originally constructed by Parrinello and Ercolessi [27]. This program uses a 5th-order predictor-corrector algorithm for solving the equations of motion, and has many facilities for "slab" simulations. We present here the results for $N = 500$.

In what follows, the physical properties are expressed either in the reduced units or in the real units suitable for argon. For the former,

we measure energy in ϵ_0, length in σ, temperature in $\frac{\epsilon_0}{k_B}$, with k_B being the Boltzmann constant, pressure in $\frac{\epsilon_0}{\sigma^3}$ and time in $(\frac{m\sigma^2}{\epsilon_0})^{\frac{1}{2}}$, where m is the mass of particles. For the latter, we substitute $\epsilon_0 = 125K$, $\sigma = 3.446\mathring{A}$ and $m = 39.9g/mol$ into the reduced units. It's well known that the LJ potential serves as a good approximation for rare gas materials, and this is particularly the case for argon. A time step is taken to be $0.00234(\frac{m\sigma^2}{\epsilon_0})^{\frac{1}{2}}$, which corresponds to $0.5 \ 10^{-14} sec$. for argon.

We start with an f.c.c. structure. The reason why we choose an f.c.c. crystal as our initial structure is that argon is known to form an f.c.c. crystal below $84K$. In our constant pressure-constant temperature simulation, the system adjusts itself so that it can take the structure and the volume which it should take under given temperature and pressure. However, the energy barrier among the f.c.c. and h.c.p. structures is fairly high, our system once constructed in a f.c.c. structure, does not transform to an h.c.p. structure. At each temperature we initially set the compensating pressure according to equation 2.7, with the density calculated by using the lattice constant obtained by extrapolating those at lower temperatures (for $T = 0$ we use a trial lattice constant). The system could however reach an equilibrium point corresponding to a different density, thereby making invalid the initial choice for the compensating pressure. For this reason, in the course of the simulation we continuously monitor the lattice constant, and adjust the compensating pressure whenever the lattice constant is changed appreciably from the initial one in order to achieve self-consistency. Changes in the pressure during the run are rather small anyway, being typically contained within $\sim$ 5% at $T = 0.72$, and practically zero at low temperatures ($T < 0.60$), where the temperature dependence of the lattice constant is nearly linear.

Starting from $T = 0$, we increase the temperature of this f.c.c. crystal up to $T = 0.84$ with each increment of 0.08. At each temperature, we have equilibrated the system for 5000 steps, calculating the desired statistical quantities as time averages. We present the compensating pressure and atomic volume as a function of temperature, respectively
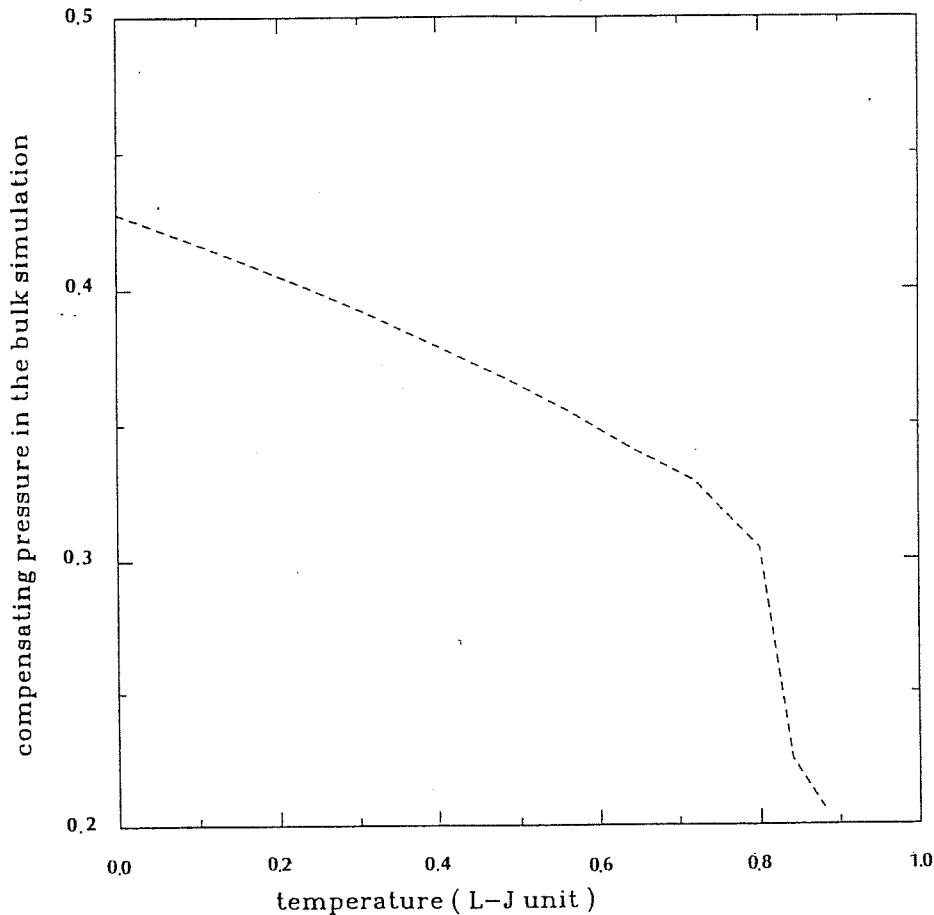
16

Figure 2.1:

Compensating pressure (in reduced unit) used in the bulk simulation (see equation 2.7).

in Figs. 2.1 and 2.2. Other data, including one-particle energies and lattice constant, are reported in table 2.1. Note that the lattice constant serves as input for the surface simulation described in the next chapter. From fig. 2.2, we can locate the bulk melting point somewhere between 0.72 and 0.84 reduced unit. Due to the unavoidable presence of overheating, T_m is probably closer to the former values. The problem of determination of T_m will be discussed in chapter 3. The correlation function (see fig. 2.3) shows a gradual disappearance of the second peak inside this temperature range, indicating loss of f.c.c. crystalline order.

Nosé and Yonezawa [40], who have studied a LJ system with a cutoff distance $r_c = 2.9$ and a compensating pressure $P = 0.593$ reduced unit (250bar), also estimated the bulk melting point to be 0.84 (105K). Both calculations are limited by the finite size of the simulation system and

17
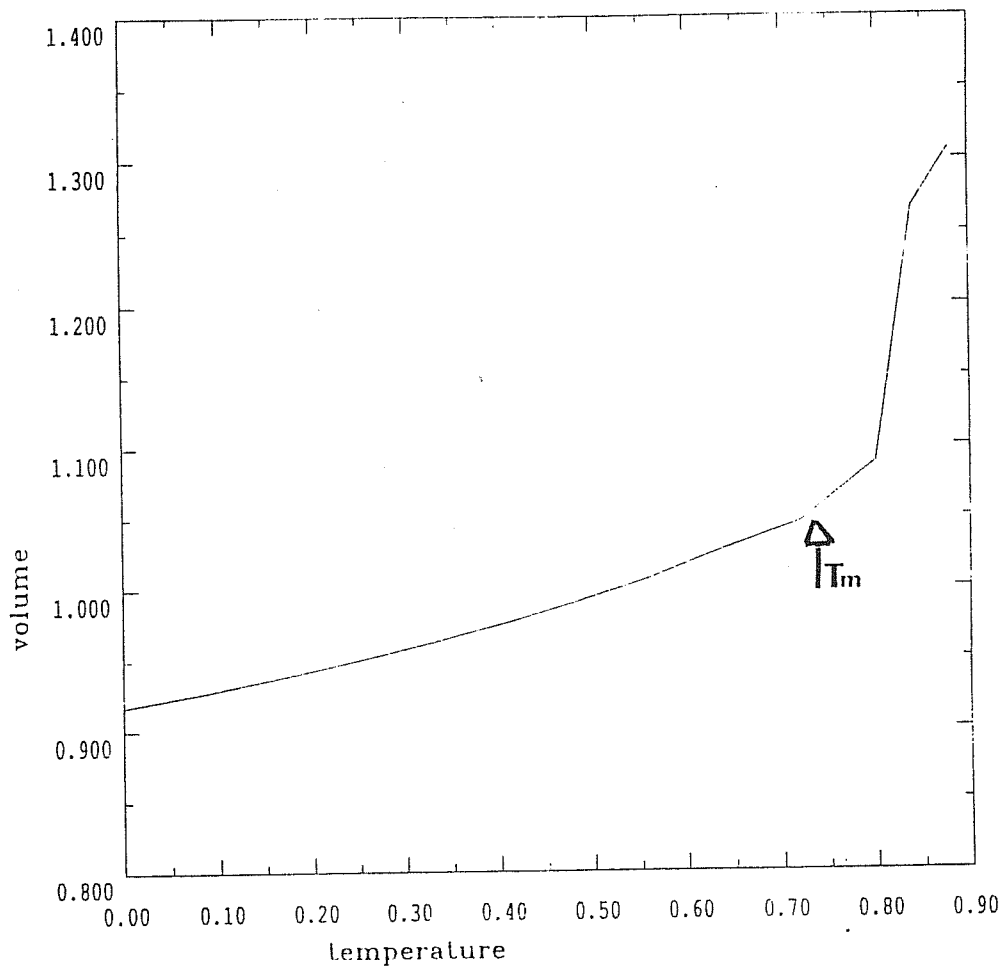
Figure 2.2:

One particle volume (in reduced unit) thermal expansion.

Temperature	E_{sr}	E_T	E_{kin}	E_{tot}	a	ρ	P
0.00	−8.300	−0.671	0.001	−8.970	1.5422	1.091	0.43
0.08	−8.182	−0.664	0.121	−8.725	1.5476	1.079	0.42
0.16	−8.059	−0.657	0.241	−8.475	1.5534	1.067	0.41
0.24	−7.932	−0.649	0.239	−8.342	1.5596	1.055	0.40
0.32	−7.795	−0.641	0.481	−7.955	1.5664	1.041	0.39
0.40	−7.650	−0.632	0.601	−7.681	1.5738	1.027	0.38
0.48	−7.493	−0.622	0.721	−7.392	1.5819	1.010	0.37
0.56	−7.322	−0.611	0.842	−7.091	1.5910	0.993	0.36
0.64	−7.128	−0.599	0.962	−6.765	1.6017	0.974	0.34
0.72	−6.932	−0.588	1.082	−6.438	1.6114	0.956	0.33
0.80	−6.604	−0.566	1.202	−5.968	1.6326	0.919	0.30

Table 2.1:

One particle short-range potential energy E_{sr}, tail potential energy $E_T = \alpha\rho$, kinetic energy E_{kin} total energy $E_{tot} = E_{pot} + E_T + E_{kin}$, lattice constant a, and particle density ρ and compensating pressure $P = -\alpha\rho^2$, as a function of temperature. All quantities are expressed in reduced units.
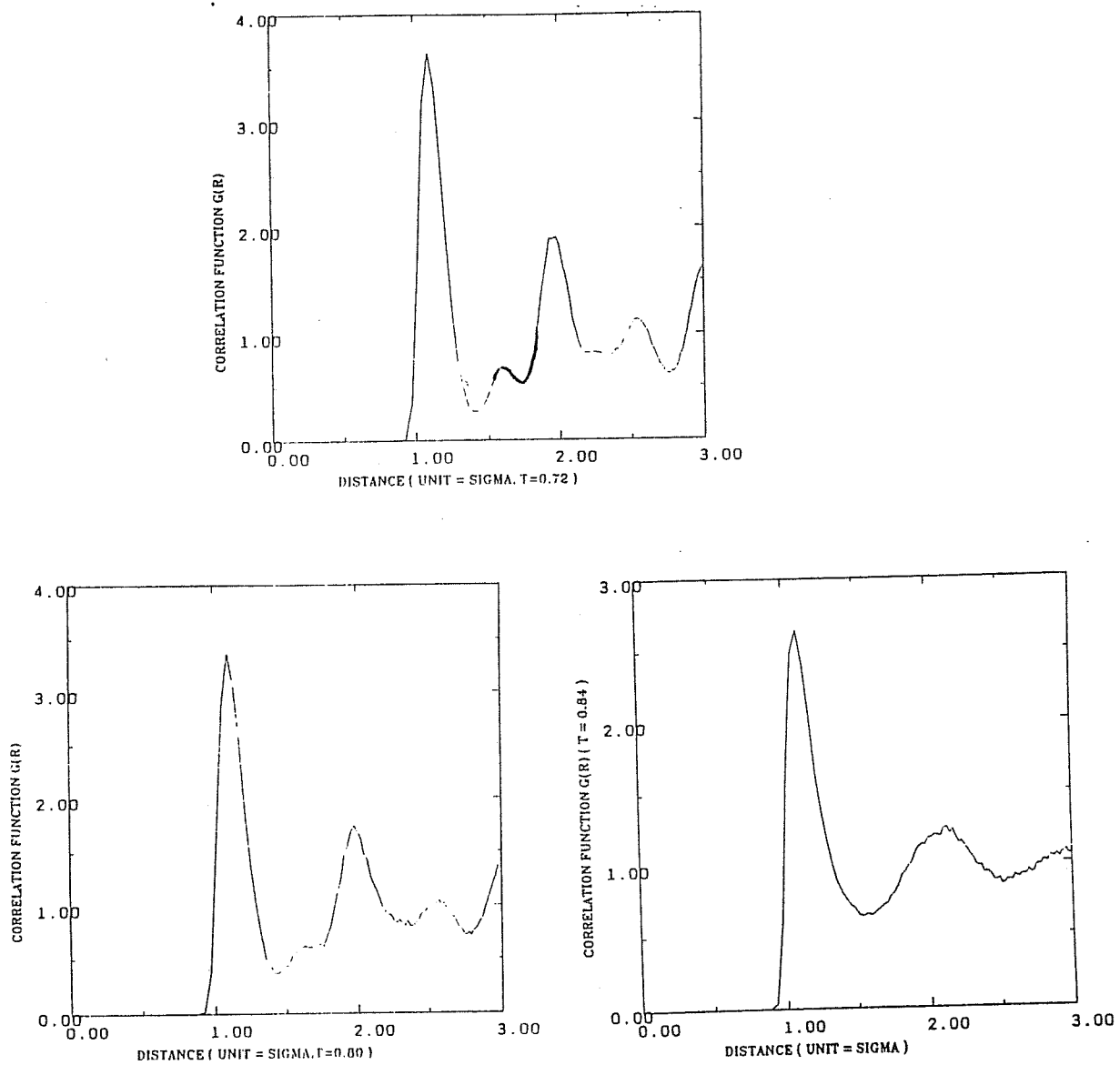
Figure 2.3:

Bulk correlation function at temperatures $T = 0.72, T = 0.80$ and $T = 0.84$. Reduced units are used.

the finite simulation time. Due to the unavoidable presence of hysteresis, implying superheating, the value 0.84 is thus considered as an upper bound for the melting point. A more precise determination of $T_m \sim 0.74 \pm 0.02$ has been obtained by studying a system with a free surface, as described in the following chapter.

Chapter 3

Surface Simulations

3.1 Method

3.1.1 A "semi-infinite" slab

The usual geometry utilized in simulation for surface studies is the "slab": a system with two parallel free surfaces, separated by an adequate thickness of material. By this, we mean that the thickness should be large enough so as to make the surface quantities we are measuring independent of the thickness itself, i.e. well converged to their limit value corresponding to an infinite thickness. Therefore, the slab is nothing but a computational device, which avoids us the difficulty of directly studying a semi-infinite system, which is what physically interests us. This trick works well for a large number of things, such as surface phonons in crystals, multilayer relaxations etc.. In all these cases, surface effects decay relatively quickly when moving from the surface into the bulk. However, we expect the slab model to work badly in our case, where tail interactions coming from the deep bulk are supposed to have important effects at the surface. For this reason, the slab model has to be replaced by something which more closely approaches a semi-infinite system.

Our simulation system is still a slab, but its two surfaces are treated in a different way. One of them is the free surface, which is the subject of our study. The other surface is seen as an interface towards an infinite
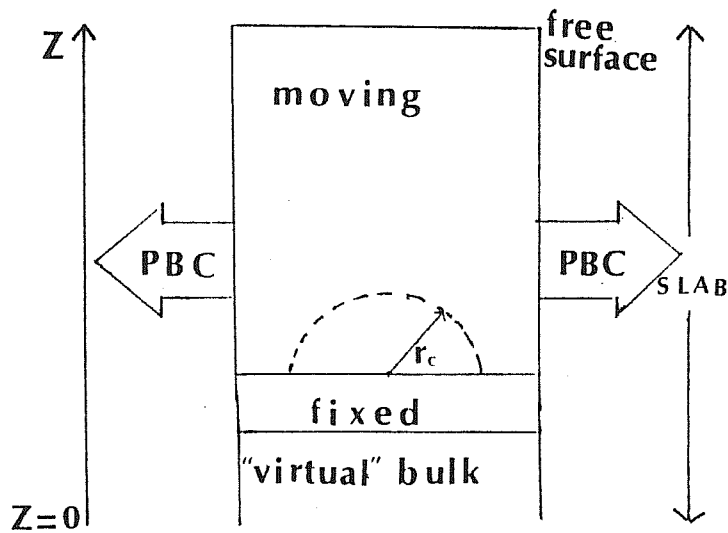
Figure 3.1:

The geometry used for surface studies (see text).

bulk (see figure 3.1). On this side, a thickness of material at least equal to the force cutoff distance r_c is kept fixed, with the atoms frozen at perfect lattice positions and not subjected to dynamics. These fixed atoms have the purpose to supply realistic bulk-like short-range forces to the moving atoms just above. The thickness of this fixed material (at least r_c) ensures that no moving atom can "see" the bottom surface, that is, there are not large density anisotropies within a sphere of radius r_c centered on each moving atom. To minimize internal stress effects, the lattice parameter of the fixed lattice is that of a pure bulk at the same temperature we wish to simulate on the system with the surface, and is taken from the bulk simulation described in chapter 2.

Outside a sphere of radius r_c centered on each atom, the system is treated as a uniform fluid and the forces are obtained by integration. In this case, we explicitly assume a semi-infinite system, leading to the formulas in section 3.1.2. This amounts to assume the presence of a "virtual" bulk below the fixed atoms (Fig. 3.1). Overall, this system behaves as semi-infinite, with the exception of the atoms in contact

23

with fixed atoms. Here, the dynamics is severely different from that of a real semi-infinite system. This effect, however, is related to an approximation on short-range forces, and we expect it to be relevant only within distances of the order of r_c from the fixed part. This becomes unimportant if we make the total "moving" slab thickness much larger than that. Long-range effects on the other hand, which worried us in the first place, are now correctly treated, so that atoms near the free surface "feel" tail contributions from an underlying semi-infinite bulk.

Finally, note that the crystalline fixed substrate has a practical advantage in avoiding a complete melting of the system even above the bulk melting point, and supplying a "crystal seed" which is crucial to recrystallize the system if the temperature is decreased. This allows us to study easily the system in both directions (solid to liquid, T increasing, and liquid to solid, T decreasing), obtaining both the lower and upper boundary of the hysteresis cycle when measuring, for instance, the number of molten layers as a function of T.

3.1.2 Tail force and energy

In our surface studies, PBC are in effect only along directions parallel to the surface plane (x and y directions), whereas free conditions are used along the surface normal (z direction). As described in chapter 1, we split the forces into a long-range part and a short-range part. The short-range interaction is treated directly with the normal discrete sum (see equation 1.16). Contrary to the bulk simulation case, the long-range interaction tail gives an important contribution to the force in surface simulations. For simplicity, we approximate again the discrete sum in equation 1.18 by:

$$\vec{F}_2(r_i) \simeq \int d\vec{r'} \rho(\vec{r'} + \vec{r_i}) \frac{1}{r'} \frac{d\phi_T(r')}{dr'} \vec{r'} \theta(r' - r_c). \qquad (3.1)$$

Now the difficulty lies in the fact that our system is not homogeneous, since the solid, liquid and vapor phases may coexist, and several approximations for $\rho(\vec{r})$ have to be done to make the calculation of the integral practically possible. First of all, we assume all the interfaces

24

between phases to be planar. This is partially justified by the use of a MD box repeated by periodic boundary conditions, which automatically suppresses fluctuations of the interface along z direction (normal of the free surface) with wavelength larger than the box size. Moreover, we assume that the particle density depends only on the z coordinate. In the end, to be able to analytically integrate out this term, following Gibbs [41], we approximate the density function with a step form:

$$\rho(z) = \begin{cases} \rho_1 & \text{if } z \leq z_0; \\ \rho_0 & \text{otherwise.} \end{cases} \tag{3.2}$$

The plane parallel to the step $z = z_0$ is called Gibbs plane, and ρ_1 and ρ_0 are parameters determined by the density profile of the system. The Gibbs plane is a reference plane throughout our surface simulation. This is a common approximation, used by people for studying surface excess quantities. Of course, it is not at all justified a priori, and can easily rise up controversy. We'll discuss this point in detail in chapter 4, where we describe an improvement over this approximation, together with a brief description of simulations in course, based on the improved method. Anyway, for our present academic purposes, the step form is not completely unreasonable, and amusingly, it turns out that with this simplified model, we get a remarkably good agreement with the theoretical expectations and experimental results (see section 3.5.2).

With these simplifications, $\vec{F}_2$ is reduced to the following analytic form:

$$\vec{F}_2(z_i) = \begin{cases} \hat{z}2\pi(\rho_1 - \rho_0)f_2(|z_0 - z_i|), & \text{if } |z_i - z_0| \leq r_c; \\ \\ \hat{z}2\pi(\rho_1 - \rho_0)\{f_2(r_c) \\ + \frac{1}{2}\phi(r_c)[r_c{}^2 - (z_0 - z_i)^2]\}, & \text{otherwise.} \end{cases} \tag{3.3}$$

where

$$f_2(x) = -\frac{1}{2}\frac{a}{(x+b)^2} + \frac{ab}{3}\frac{1}{(a+b)^3}. \tag{3.4}$$

Here, $\hat{z}$ is the positive direction chosen as the normal of the free surface, z_0 is the Gibbs plane position, calculated by fitting the real density to a step function as discussed below, and z_i is the z coordinate of particle i.

The tail contribution to the one particle energy is just the integral of $\vec{F_2}$. We get, after some straightforward algebra

$$
\begin{aligned}
V_T(z_i) &= V_1(z_i) \\
&\equiv -2\pi(\rho_1 - \rho_0)\left(\frac{a}{(z_i - z_0 + b)} - \frac{ab}{3}\frac{1}{(z_i - z_0 + b)^2}\right) ; \quad (3.5)
\end{aligned}
$$

for $z_i \geq z_0 + r_c$,

$$
\begin{aligned}
V_T(z_i) &= V_2(z_i) \\
&\equiv V_1(z_0 + r_c) - 2\pi(\rho_1 - \rho_0) \\
&\quad \left(\left(f_2(r_c) + \frac{1}{2}\phi_T(r_c)r_c^2\right)(z_i - z_0 - r_c)\right. \\
&\quad \left. -\frac{1}{2}\phi_T(r_c)\frac{1}{3}[(z_i - z_0)^3 - r_c^3]\right) ; \quad (3.6)
\end{aligned}
$$

for $z_0 - r_c < z_i < z_0 + r_c$, and

$$
\begin{aligned}
V_T(z_i) &= V_3(z_0 - r_c) \\
&\equiv V_2(z_0 - r_c) - \\
&\quad 2\pi(\rho_1 - \rho_0)\frac{1}{2}\left[\frac{a}{z_i - z_0 - b} + \frac{ab}{3}\frac{1}{(z_i - z_0 - b)^2}\right. \\
&\quad \left. +\frac{a}{r_c + b} - \frac{ab}{3}\frac{1}{(r_c + b)^2}\right] . \quad (3.7)
\end{aligned}
$$

for $z_i \leq z_0 + r_c$.

An alternative, but equivalent way of calculating the tail energy is to directly integrate the tail potential:

$$
V_T(\vec{r_i}) = \frac{1}{2}\int d\vec{r'}\rho(\vec{r'})\phi(|\vec{r'} - \vec{r_i}|)\theta(|\vec{r'} - \vec{r_i}| - r_c), \quad (3.8)
$$

with $\rho(\vec{r})$ approximated in equation 3.2. The derivatives of V_T gives out two terms: one term is that defined in equation 3.3; another term, arised due to the derivatives of the heaviside function, is cancelled by its short-range counterpart.

The tail contribution to the force and the one-particle energy are plotted in fig. 3.2. We see that the tail correction acts as an external field, the force is extremely long ranged, something like 10 σ, and is
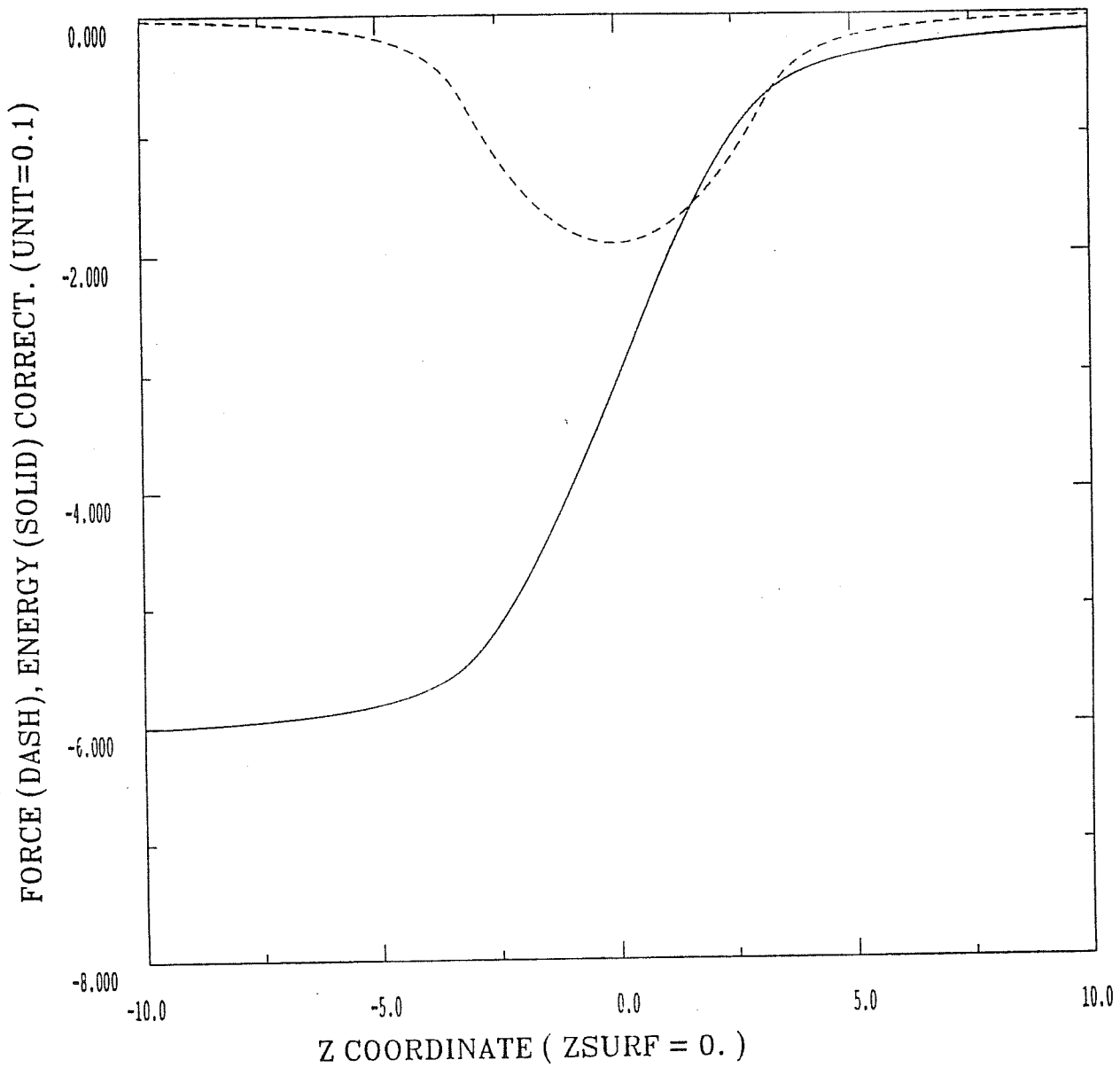
Figure 3.2:

Tail force (dash line) and energy (solid line) as a function of z. The Gibbs plane of density corresponds to $z = 0$ in this figure. Reduced units are used.

largest in the interphase region (near the Gibbs plane). This force tends to keep the particles from evaporating away from the surface, i.e. it rises up the energetic barrier between the liquid phase and the vapor phase. Also, the energy contribution of tail interaction lowers the total energy (in practice, this is as large as ten per cent, see table 3.2).

To construct the tail force, we have at first constructed the density profile via simple histogram statistics, with a histogram width equal to $\frac{1}{11}$ of the lattice constant. In order to have an accurate fitting, we have then smoothed out the density profile obtained in this way, by averaging over a window of 11 histogram channels centered on each channel. Then we fit the new smoothed histogram to a step function by using the standard χ^2 criterion. The plane corresponding to the step position is then taken as the Gibbs reference plane. The whole procedure is repeated at each time step, so that the reference plane can move during the simulation run.

3.1.3   The reflection wall

In the course of simulation, some particles appear to evaporate away. In order to avoid a loss of particles (which cannot be replaced in our canonical simulation), we have imposed a reflection wall above the Gibbs reference plane. The distance between the two planes is changed from one temperature to another, and is adjusted to be large enough to not affect too much the system (by the presence of the wall), but also small enough to avoid excessive equilibration times. In practice, it turns out that for $T \leq 0.60$, the reflection wall is of no use, since no particle is observed to evaporate, while at $T = 0.76$ we put the reflection wall at about 4σ above the Gibbs plane.

The reflection wall works in the following way. Suppose during the simulation, one particle goes beyond the reflection wall. Due to numerical integration by discrete time steps, when this event is detected the particle will have its coordinate (z-component) $z = z_{rf} + \Delta z$, where z_{rf} is the coordinate of the reflection wall and $\Delta z > 0$. If v_z is the z-component of the velocity, the wall will elastically mirror-reflect the
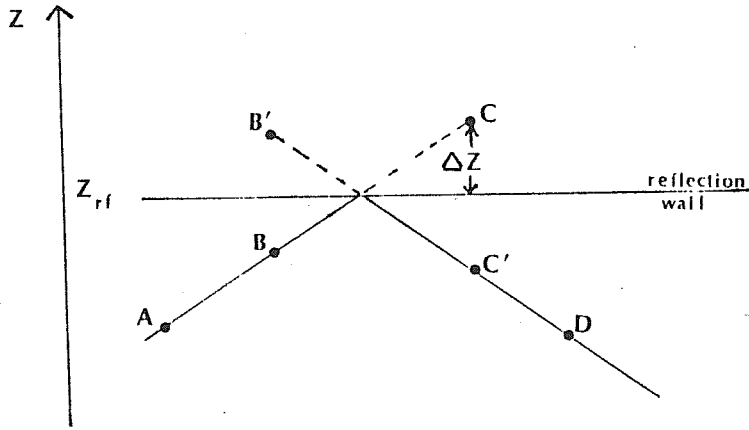
Figure 3.3:

Dynamics of a reflection event. The dots represent the positions assumed by the particle at successive integration time steps. The particle proceeds through $ABC\cdots$, but at C it is detected to be above the reflection wall. The reflection procedure moves the particle in C' and inverts its velocity along z. The integration algorithm remains essentially unaware of the event, and proceeds to calculate the trajectory $C'D\cdots$ as though particle were coming from B'.

particle by transforming

$$z \;\rightarrow\; z - 2\Delta z$$
$$v_z \;\rightarrow\; -v_z \tag{3.9}$$

While the inversion of v_z is quite obvious, the correction to z is required to ensure a smooth operation of the integration algorithm throughout the reflection event (see fig. 3.3).

3.1.4 Construction of the system

Our simulation system is composed of 1600 particles, of which 1300 are moving and 300 are fixed to mimic the bulk solid. Each crystal layer consists of 50 particles, so that we have a total of 32 layers, of which 6 layers are fixed. The number of fixed layers is chosen in such

a way to correspond to a total thickness (3.8555σ at zero temperature) larger than the cutoff distance r_c (see equation 3.3). We have chosen as initial structure, a f.c.c. crystal with a (100) free surface, which is expected to be easy to melt [22]. Generally, surface simulations are more time consuming, because of the larger number of particles, and longer equilibration times. Thus, to speed up the surface simulations, we have increased the time step to 0.004 reduced units, corresponding to $0.86\ 10^{-14}sec$. No appreciable errors appeared for this increase. At each temperature step, we set the lattice constant a equal to that obtained in the independent bulk crystal simulation described in chapter 2.

3.2 Low temperature results

3.2.1 Surface disordering

We have carried out simulations on surface melting by first creating the crystal with the structure described in the previous section. In the initial configuration, the distances between layers are all equal to the bulk inter-planar distance. This configuration, however, does not correspond to an energy minimum at $T = 0$. In the equilibrium state, the spacing between layers near the surface is usually fairly different from the bulk inter-planar distance. For this reason, our initial configuration intrinsically contains an amount of extra potential energy that, when the simulation is started, results in an oscillatory motion along z of the whole slab with a rather long period. To avoid this undesirable effect, we first relax the system by quenching it for 250 steps. In this run, all particle velocities are rescaled at each time step by a factor $\alpha = 0.5$. This run allows the layers to relax and brings the system closer to its energy minimum.

At this point, the positions are randomized and we heat up the crystal to 0.36 reduced temperature units, with each increment of temperature $\Delta T = 0.12$, and equilibrate the system for 4000 time steps. Up to $T = 0.36$, every property of the crystal shows a solid-like behavior. We then proceed to $T = 0.48$, and equilibrate it for 6400 steps. At this
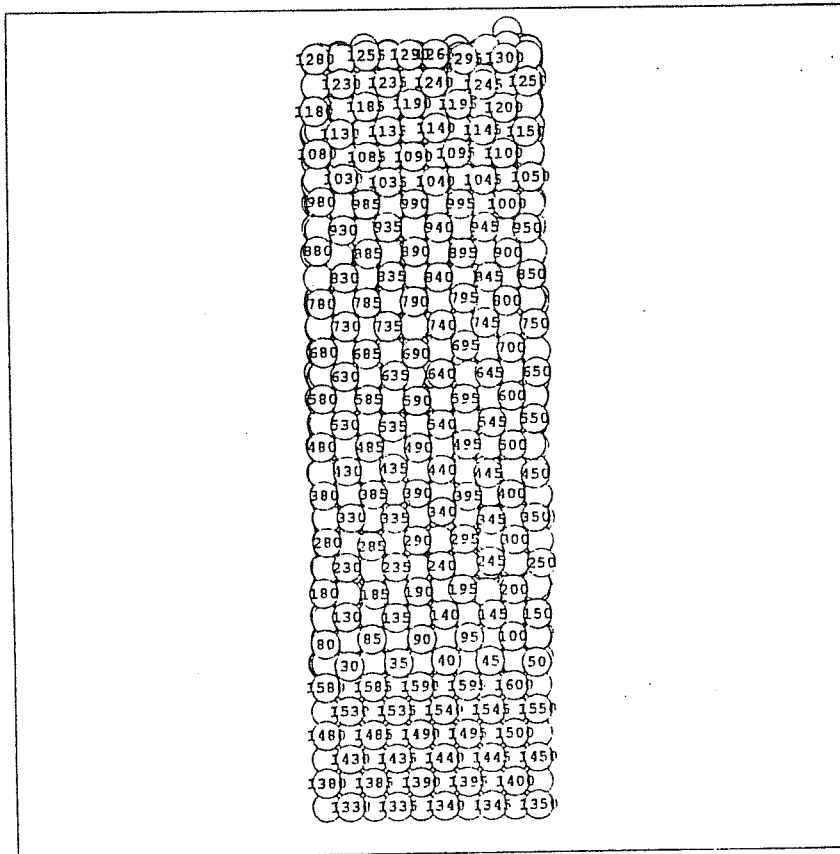
30

Figure 3.4:

Instantaneous lateral view of the crystal structure at $T = 0.48$ reduced units.

temperature, some atoms of the top layer have been promoted over the reference plane. Since the temperature is still far from the triple point ($T_m \simeq 0.74$, see section 3.5.1), these particles have not enough kinetic energy to overcome the attractive force due to the other atoms, and so they just oscillate near the top layer. In other words, they are just adatoms. These oscillations originate fluctuations of the "vapor" density and oscillations of the reference plane, slowing down the equilibrium process. The formation of adatoms can be visualized from figure 3.4, where instantaneous positions of the particles are sketched. In figure 3.5 we see

31
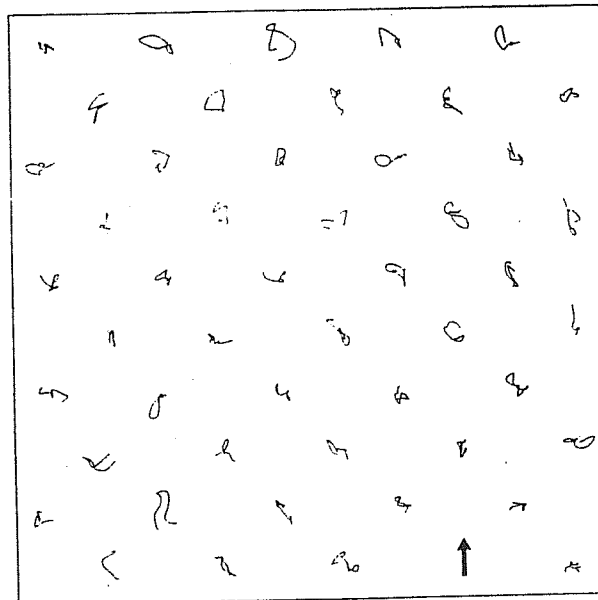
RUII OF 88/06/13 12.17.59. FOR LJ
REF : MELTING

PLOT FROM STEP   0 TO STEP   300, POSITIONS TAKEN EVERY 10 STEPS
PLOTTING SLICE PARAMETERS :   ORIENTATION (0.000   0.000   1.000) -
        X-AXIS (1.000   0.000   0.000) - Y-AXIS (0.000   1.000   0.000) -
        CENTER   0.0000   0.0000 12.5056 - THICKNESS   0.7000 - SIZE   8.0000

Figure 3.5:

x-y projected trajectories of the particles in the top layer within 300 time steps ($T = 0.48$). The free surface normal is toward the reader. Note the vacancy indicated by an arrow.

the trajectory of the particles of the top layer over 300 time steps. Note the presence of a vacancy. A plot of the density profile (see figure 3.6) shows an increase of width of the top layer, and a small secondary peak due the presence of adatoms.

3.2.2 A specific heat peak

The total energy E_{tot} is another quantity from which we can get some interesting thermodynamic informations. We have plotted the total energy as a function of temperature (see figure 3.7).

There is a step-up between 0.36 and 0.48. The origin of this step in the total energy is still uncertain. It corresponds to a peak in the specific heat (see figure 3.8). Theoretically, soluble models also show a specific heat peak at some 20% below roughening temperature [43,11] T_R. It is generally accepted that MD simulations can not reproduce the roughening transition, because the finite simulation size limits the fluctuations. However, the specific heat peak is associated in the models,
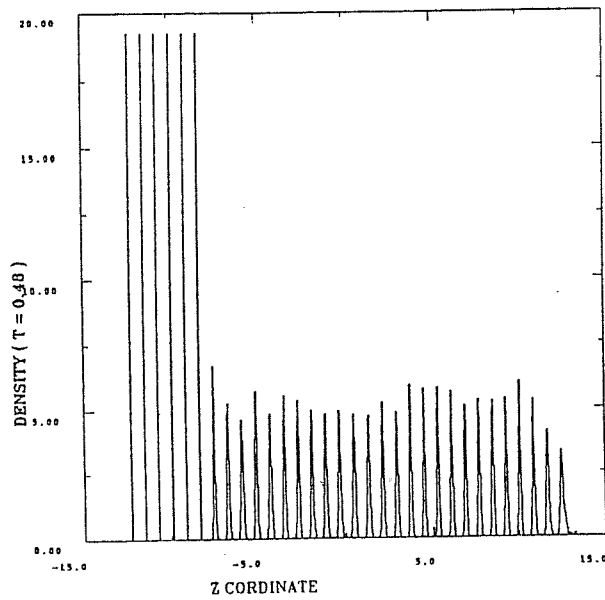
Figure 3.6:

(x, y) averaged number density profile (along z direction) at $T = 0.48$. The first six layers on the left-hand side are rigidly frozen at their ideal bulk positions.
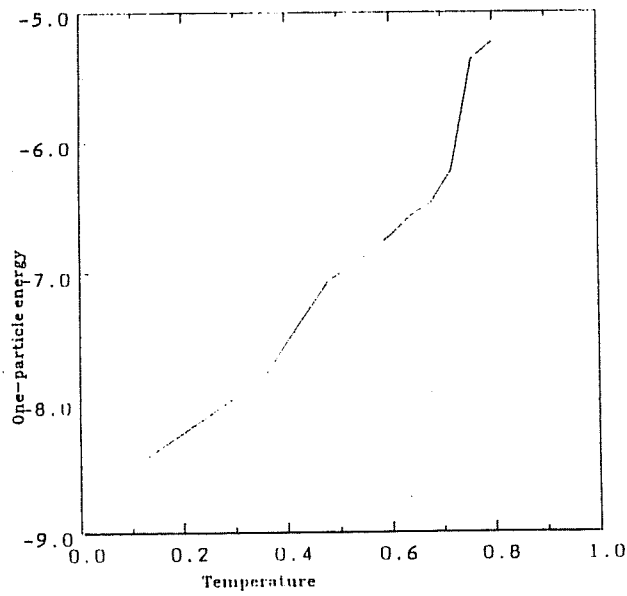

Figure 3.7:

Total energy per particle (in reduced unit) as a function of temperature.
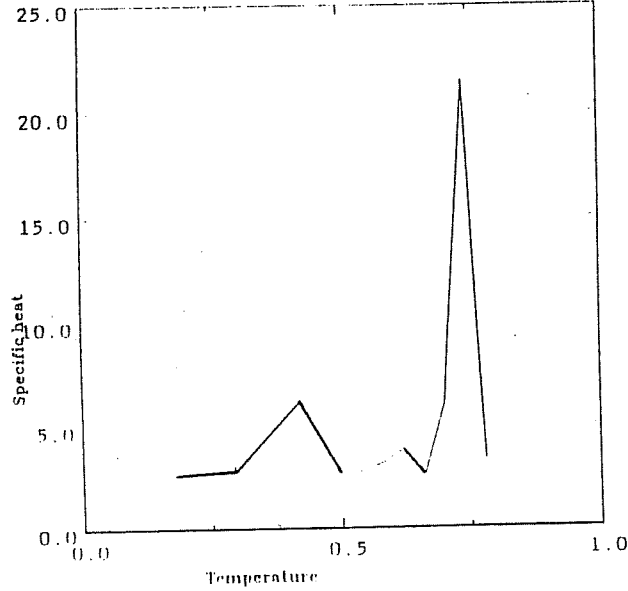
33

Figure 3.8:

Specific heat as a function of temperature. Reduced units are used.

with the loss of vertical short-range order, and that can very well be re-produced in a simulation. The situation is still somewhat unclear, as for example the entropy increase around $T \sim 0.42$ extractible from Fig. 3.8, seems one order of magnitude too large to fit into this explanation. In attempt to understand the situation, we have plotted the density difference $\rho_d = \rho_1 - \rho_0$ as a function of temperature (see figure 3.9). At $T = 0.36$, $\rho_0 = 0$ and ρ_d is just the number density of the solid phase. At $T = 0.48$, due to the presence of adatoms, ρ_0 is increased to 0.6, while ρ_1 is decreased due to thermal expansion of the lattice. This suddenly increases the tail potential energy (see equation 3.5,3.6, 3.7). Whether this is an artefact of our step approximation of the density profile, or it is due to the effect of the long range tail is unclear. Probably both are the origin. On one hand, since the adatom "layer" is very thin, the smoothing of density profile (see section 3.1.2) significantly rises up the adatoms density and so artificially lowers ρ_d. However this cannot be the only factor for the sharp decrease of ρ_d, in view of the flat valley of ρ_d between $T = 0.48$ and $T = 0.64$, which means that $\rho_d(T = 0.48)$
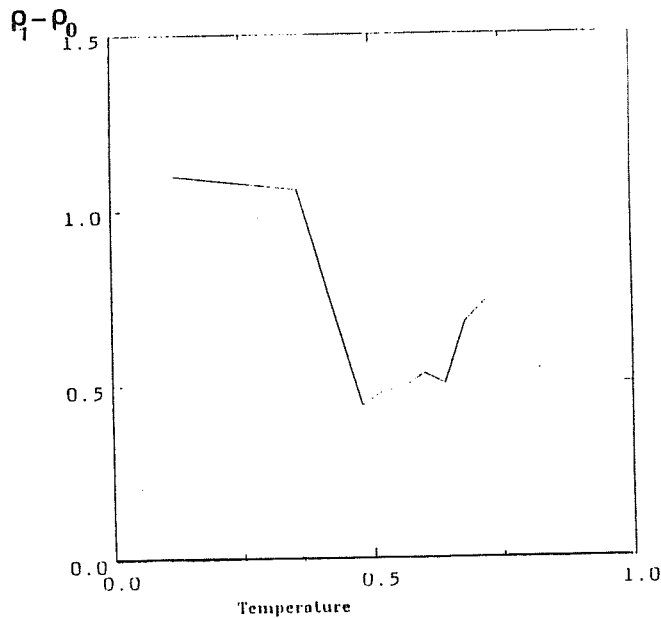
34

Figure 3.9:

Density difference $\rho_d \equiv \rho_1 - \rho_0$ as a function of temperature. Note that, due to the step approximation of density profile, in ρ_1 there are contributions from both solid and liquid particles, just as in ρ_0 there are liquid and vapor particles.

should not be too much off.

A simulation without the step approximation, to check this point and other interesting behaviors, is presently in progress (see chapter 4). This radically improved description of the interface, should enables us to eliminate the uncertainties discussed above.

3.3 Intermediate temperature results: formation of the quasi-liquid layer

We heat further the system up to $T = 0.56$, by setting the increment of temperature $\Delta T = 0.04$ reduced units. At each temperature we have equilibrated the system for 7000 time steps. In the course, the number of adatoms increased continuously, so that at $T = 0.56$, a film of quasi-liquid is already formed as the plot of density profile (see figure 3.10) suggests. Figure 3.11 (trajectory plot) shows the evidence of some in-plane diffusion. It is interesting to see that the formation of this quasi
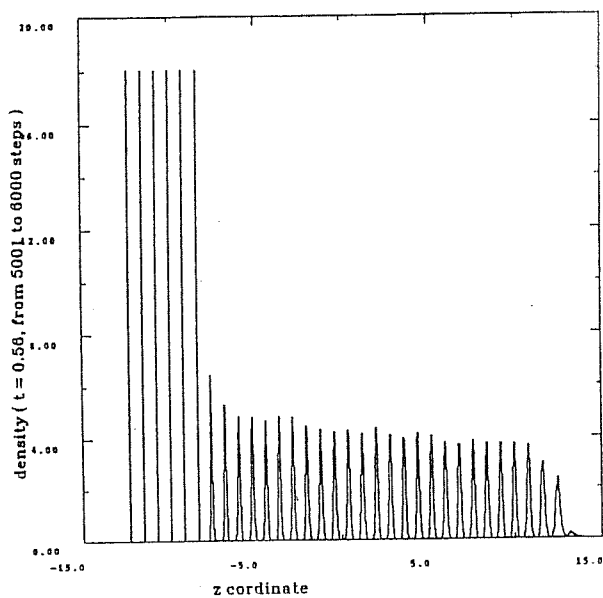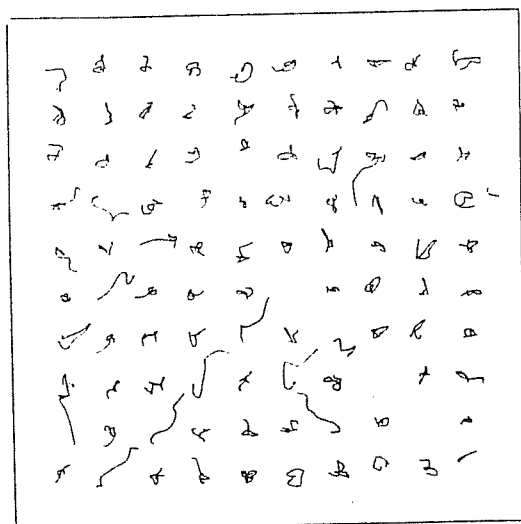
Figure 3.10:

Number density profile at $T = 0.56$

Figure 3.11:

Trajectory of the atoms in the quasi-liquid layer at $T = 0.56$ within 300 time steps. Note the surface diffusion processes.

liquid film is gradual (from $T = 0.48$ to $T = 0.56$) and smooth. While the energetic cost associated with the creation of the first adatoms at $T = 0.48$ is surprisingly high (see discussion in section 3.2.2), continuing to form the quasi-liquid film is fairly easy.

3.4   Definition of molten layers

There are several qualitative and semi-quantitative ways to define a molten layer :

1. The intra-layer pair correlations have lost their crystalline shell structure;

2. The mean square displacement is linear with time and large;

3. The average energy per atom is sensibly larger than in a typical bulk layer;

4. The in-plane orientational order O_4 (see below) has dropped from close to one to close to zero.

We define

$$O_4 = \frac{|\sum_{ij} W_{ij} e^{4i\theta_{ij}}|}{\sum_{ij} W_{ij}}. \tag{3.10}$$

Where the sums run over first-neighbor pairs and θ_{ij} is the angle which the $i - j$ bond, projected to xy plane, forms with the x axis. The weight function

$$W_{ij} = exp\left(-\frac{(z_i - z_j)^2}{2\delta^2}\right), \tag{3.11}$$

with δ half of the average inter-planar spacing, has the purpose of filtering out all "non-coplanar" neighbors. As an example, we present the behavior of O_4 (figure 3.12) and of the density profile (figure 3.13) at $T = 0.72$ reduced units.   At this temperature, crystalline layers have $O_4 \sim 0.6$, while O_4 drops to ~ 0.1 or less in the liquid phase. As a practical criterion, we call "solid" a layer with O_4 larger than 0.3 and liquid otherwise. We have checked that this generally fits well with the other criteria above. In particular, diffusion sets in rather sharply for
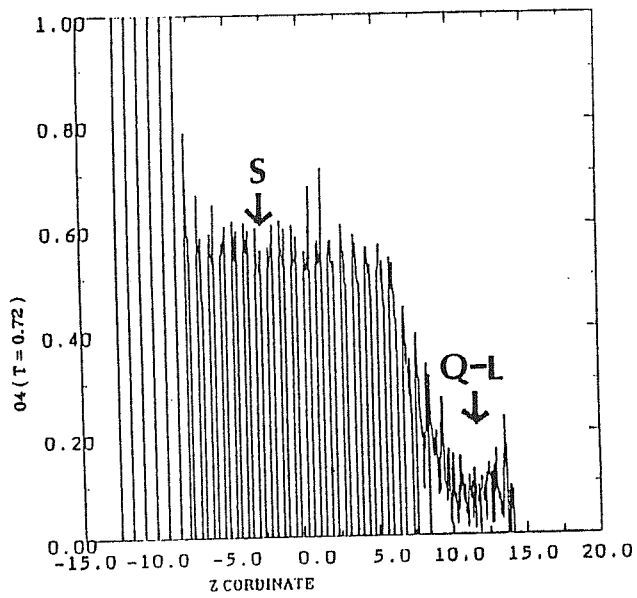
37

Figure 3.12:

Typical behavior of O_4 for the quasi-liquid (Q-L) layer on top of the solid (S) $(T = 0.72)$.
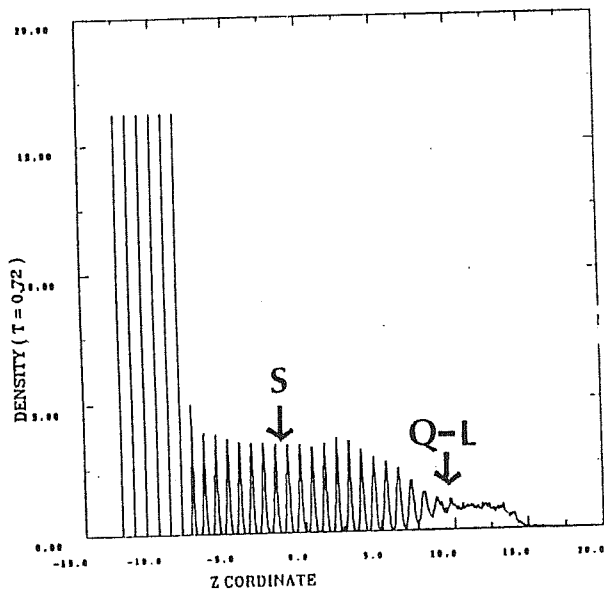

Figure 3.13:

Number density profile at $T = 0.72$.

O_4 smaller than this value, whereas for $0.3 \leq O_4 \leq 0.45$, the diffusion coefficient oscillates in time, following the fluctuations of the solid-liquid interface.

3.5 High temperature results

3.5.1 Surface melting

Using the criteria above, the results for the simulations at higher temperatures can be thus summarized: By heating up the system to $T = 0.60$ reduced unit, for 7000 steps, one layer melts. From $T = 0.60$ to $T = 0.64$, the quasi-liquid phase grows logarithmically (see section 3.5.2 and [15]). At $T = 0.64$, we have equilibrated the system for 22000 steps and a quasi-liquid layer of thickness corresponding to 3 solid layers is observed. At $T = 0.68$, particles in the vapor phase begin to appear, so that the vapor pressure becomes measurable, although with large fluctuation. (Note near the melting point, a small shift in T corresponds to a fairly large change in P.)

We have calculated the vapor pressure by defining it as

$$P = \frac{1}{AT_s} \sum_{i=1}^{n_c} 2mv_i, \qquad (3.12)$$

where n_c is the number of particles that have been reflected by the reflection wall during the simulation time T_s, v_i is z-component of the velocity of particle i and A is the area of the reflection wall (i.e., the slab area).

Special care should be paid for attainment of equilibrium at $T = 0.68$. In fact, after 20000 time steps of equilibration time, three quasi-liquid layers are formed, with one more layer beginning to melt (in this layer $O_4 = 0.36$). After other 7000 steps of simulation, this layer is also melted. This shows that the kinetics of the process is relatively slow on the MD time scale.

There is a step-up of ρ_d at $T = 0.68$ (see figure 3.9). This means that the Gibbs plane is shifted towards the gas phase so that the density difference rises due to the decrease in ρ_0.
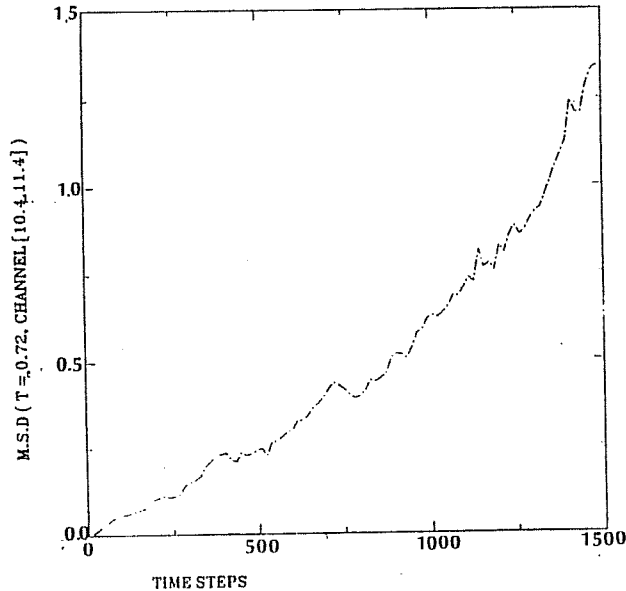
Figure 3.14:

Planar mean square displacement of a characteristic liquid "layer" (fourth layer from the top) at $T = 0.72$. Fitting the data by linear regression, we obtained the coefficient of diffusion $D = 0.05\sigma(\epsilon/m)^{1/2}$. Note the poorly converged linear regression, which might be attributed to the oscillations of the Gibbs reference plane.

Proceeding further to $T = 0.72$, with continuous monitor and care, we observe that 8 layers have melted (see figure 3.12 and fig. 3.13). The thickness of the quasi-liquid layer corresponds approximately to 10 solid layers. The diffusion of the system (see figure 3.14) shows a characteristic liquid behavior. We have plotted also the trajectory (figure 3.15), showing a clear three phase coexistence. Table 3.1 gives a comparison of our monitored results for this temperature to those obtained by Broughton et. al. for a LJ system at $T = 0.67$. Particularly, note that the latent heat of melting we obtained is smaller, which is what we expect for the long range potential. The same is true for the difference between the bulk solid density and the bulk liquid density. It is interesting to note that while our bulk solid density is approximately equal to that of BBA, our bulk liquid density is nearer to that of bulk solid. The good agreement between the fixed bulk lattice spacing and the moving bulk one confirms that the stress at this artificial interface

40

	Present	*BBA*
Temperature	$T = 0.72$	$T = 0.67$
Bulk solid density	0.97	0.965
Bulk liquid density	0.86	0.834
Bulk solid pot. energy	−7.35	−7.266
Bulk liquid pot. energy	−6.16	−6.020
Fusion energy	1.19	1.246
Bulk lattice spacing	0.8099	
Fixed bulk latt. spac.	0.8057	

Table 3.1:

Comparison of our monitored quantities at $T = 0.72$ with those obtained by Broughton, Bonissent and Abraham (BBA) [42]. Note that the temperature at which BBA monitored is the triple point of the LJ system, $T = T_m = 0.67$, which is quite different from ours. Both systems exhibit a three phase coexistence, $T_m = 0.67$ in the BBA case, $T_m = 0.74$ in ours. Our data in the table are however given only at $T = 0.72$, which is close, but not coincident with T_m. Note also that the MD simulation of BBA limits the interactions within a cylinder of diameter 4σ and height 10σ. All the quantities are expressed in reduced units.
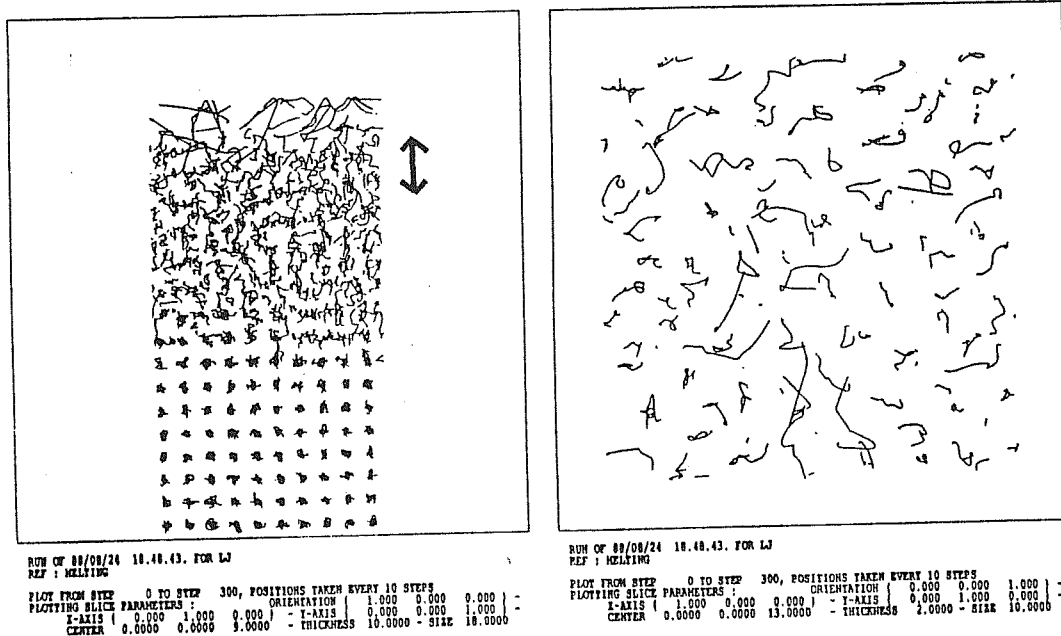
Figure 3.15:

Trajectory at $T = 0.72$, over 300 time steps. The right plot is the $(x\text{-}y)$ trajectories of particles within a slice corresponding to a thickness indicated in the left plot by a $\updownarrow$.

is small.

Heating up to 0.76, the entire crystal is melted. Thus, we are led to conclude that the triple point T_m is about 0.74, which is substantially larger than the triple point of LJ system, $T = 0.67 \pm 0.01$.

A more precise determination of T_m is very difficult, because of the intrinsic fluctuation of the temperature and the finite simulation time. We have tried to cool down the system from $T = 0.76$ to $T = 0.72$ for 40000 time steps, but the number of molten layers remained larger than that obtained by heating up. This could be attributed to the following reasons. In small systems, surface effects can cause substantial distortions of the equation of state in the vicinity of phase transition. Melting is usually a discontinuous and irreversible process. What we can say is only about the thermodynamic properties in the limited time range of about 10^{-10} to 10^{-9} seconds. A more elaborate determination of T_m is however in project now (see chapter 4). In table 3.2 we report average energies, pressures and reflection wall positions at different temperatures. Note the step-up of E_{tot} from $T = 0.72$ to 0.76 by a quantity

42

T	E_{sr}	E_{tail}	E_{tot}	σ	C_v	P_{vap}	d_{rf}	M_{ave}
0.12	-7.962	-0.638	-8.454	$0.6\ 10^{-4}$		0	24.07	500
0.24	-7.805	-0.626	-8.138	$0.7\ 10^{-4}$	2.6	0	24.28	750
0.36	-7.629	-0.613	-7.802	$1.0\ 10^{-4}$	2.8	0	24.54	750
0.48	-7.401	-0.250	-7.066	$0.8\ 10^{-4}$	6.1	0	24.66	1300
0.52	-7.322	-0.270	-6.959	$0.4\ 10^{-4}$	2.7	0	24.67	1500
0.56	-7.246	-0.283	-6.847	$0.6\ 10^{-4}$	2.8	0	24.70	1000
0.60	-7.152	-0.299	-6.720	$0.4\ 10^{-4}$	3.2	0	24.87	1000
0.64	-7.022	-0.324	-6.566	$0.6\ 10^{-4}$	3.9	0	24.95	2000
0.68	-6.895	-0.396	-6.462	$0.3\ 10^{-4}$	2.6	$1.49\ 10^{-7}$ $\pm1.49\ 10^{-7}$	25.35	3000
0.72	-6.647	-0.452	-6.221	$0.2\ 10^{-4}$	6.0	$2.63\ 10^{-7}$ $\pm1.26\ 10^{-7}$	26.21	4500
0.76	-5.938	-0.354	-5.365	$0.2\ 10^{-4}$	21.4	$1.15\ 10^{-6}$ $\pm0.26\ 10^{-6}$	28.09	4500

Table 3.2:

Some interesting quantities at several temperatures T averaged over M_{ave} time steps: the one particle short-range potential energy E_{sr}, tail potential energy E_{tail}, total energy E_{tot}, energy fluctuations $\sigma = \sqrt{\frac{<E_{tot}^2>-<E_{tot}>^2}{N(N-1)}}$, Specific heat $C_v = \frac{\partial E_{tot}}{\partial T}$ and the distance of the reference plane from the bottom of the material, d_{rf}, averaged over N time steps. Reported also the vapor pressure P_{vap}, averaged over 7000 time steps. Reduced units are used.

Temperature	0.60	0.64	0.68	0.72	0.76
thickness l	0.702	2.246	3.329	7.774	$\infty(\sim 23.127)$
$<O_4>$	0.296	0.224	0.188	0.155	0.104

Table 3.3:

Quasi-liquid layer thickness and associated orientational order parameter O_4, averaged throughout the quasi-liquid layer. Reduced units are used. Note that 0.1 is the typical value of $<O_4>$ for the liquid. At $T = 0.76$, the entire material is quasi-liquid like, except for the bottom two layers, which can not melt, due to the strong influence of the fixed bulk.

$E_{step} = 0.48$ (see figure 3.7). This is the latent heat, characteristic of the melting transition.

3.5.2 The growth of the quasi-liquid film

In Table 3.3, we report the thickness l of the quasi-liquid layer at each temperature, together with the value of O_4. The criterion used is that proposed in section 3.4.

A plot of $\log l$ versus $\log t$ ($t \equiv \frac{T_m - T}{T_m}$ with T_m varying from 0.73 to 0.75) is shown in figure 3.16. As we mentioned before, the thickness growth from $T = 0.60$ to $T = 0.64$ is logarithmic. Fitting the last three points, we get a growth law

$$l \simeq Ct^{-\eta}, \qquad (3.13)$$

with $\eta \simeq 0.77$ for $T_m = 0.74$. This is in surprisingly good agreement with the mean-field theory expectations (see section1.1) of $\eta = 1$. Care however! We have approximated the density profile by a step function (see chapter 1), which may still be reasonable for $T \leq 0.60$. As the three phase coexistence formed for $T \geq 0.68$, the step approximation becomes just an academic simplification, and can not surely take into account accurately excess quantities of the two interfaces. In fact, this simplification tends to overestimate the long-tail effect ($\eta < 1$).
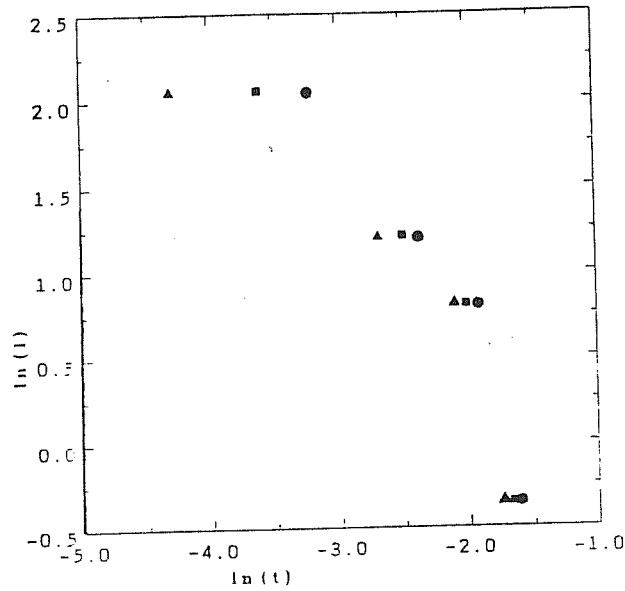
44

Figure 3.16:

The quasi-liquid layer thickness l as function of $t \equiv \frac{T_m-T}{T_m}$. As we are not able to accurately determine T_m, different curves have been plotted, corresponding respectively to a) $T_m = 0.75$ (circles); b) $T_m = 0.73$ (triangles); c) $T_m = 0.74$ (squares). The corresponding value of η extracted from these fit is a) $\eta = 0.56$; b) $\eta = 0.77$; c) $\eta = 0.96$.

Chapter 4

Discussions and Outlook

We have carried out simulations on a model system, with a long-ranged potential. Both bulk and surface simulations appear to be successful. The bulk results are physically very reasonable, and also rather close to the known behavior of, e.g., rare-gas solids [40]. Surface initiated melting has been unambiguously observed. In particular, a quasi-liquid film of 8 layers is observed near, but below T_m, which fits well theoretical expectations. In particular, mean-field calculations by Trayanov and Tosatti [39], yield qualitatively similar results on a (110) surface with the same potential used here.

A new unexpected specific heat peak has been found, at a temperature where vacancies and adatoms begin to appear. The reliability of this phenomenon is still uncertain, due to the approximations we have made. Some improvement on the tail force calculation is now in progress. This consists of directly using the equation 3.1, and treat the integral with discrete sum over z, by dividing the material into fine slices parallel to the free surface. Following the new method, the three artificially introduced dynamic quantities z_0, ρ_0 and ρ_1 will disappear. The three phase thermodynamics is thus more correctly taken into account.

Several interesting simulations are now in progress, with the following purposes:

1. Check of the specific heat peak at $T = 0.42$, which might be of importance for the understanding of roughening;

46

2. Study of the quasi liquid film growth law with the new method. With proper account of the three phase coexistence, we might be able to improve further the reliability of the results. In particular, we should be interested in the cross-over between the $\log t$ behavior and the t^{-1} behavior;

3. Determination of the phase diagram, in particular of the triple point in a more accurate way, by starting with a system of solid-vapor coexistence mixture.

4. Investigation of dynamical effects at surface melting.

Bibliography

[1] I. N. Stranski, *Z. Phys.* **119**, 22 (1942)

[2] A. Ubbelohde in *The Molten State of the matter*, Oxford, Clarendon Press (1965)

[3] D. Nenow, in *Progress in Crystal Growth and Characterization*, (Pergamon, Oxford,1984), volume 9, p. 185

[4] J. W. M. Frenken, J. F. van der Veen, *Phys. Rev. Lett.* **54**, 134 (1985);
J. W. M. Frenken, P. M. Maree, J. F. van der Veen, *Phys. Rev. B* **34**, 7506 (1986)

[5] Da-Ming Zhu, J. G. Dash, *Phys. Rev. Lett.* **57**, 2959 (1986)

[6] J. Krim, J. P. Coulomb, J. Bouzidi, *Phys. Rev. Lett.* **58**, 583 (1987)

[7] M. Bienfait, lecture at *Second International Conference on the Structure of Surface (ICSOS II)*, Amsterdam, 22-25 June (1987).

[8] B. Pluis, A. W. D. v Gon, J. W. M. Frenken, J. F. van der Veen, *Phys. Rev. Lett.* **59**, 2678 (1987)

[9] E. G. mcRae, R. A. Malic, *Phys. Rev. Lett.* **58**, 1473 (1987)

[10] S. T. Chui and J. D. Weeks, *Phys. Rev. B* **14**, 4978 (1976) and *Phy. Rev. Lett.* **40**, 733 (1978)

[11] H. van Beijeren, *Phys. Rev. Lett.* **38**, 993 (1977)

[12] J. D. Weeks, in *Ordering in Strongly Fluctuating Condensed Matter Systems*, ed. T. Riste, (Plenum Press, 1980) and reference therein. See also H. van Beijeren and I. Nolden, to be published.

[13] P. Nozieres and F. Gallet, *J. Physique* **48**, 353 (1987)

[14] J. Villain, D. R. Grempel and J. Lapujoulade, *J. Phys. F* **15**, 809 (1985);
W. Selke and A. M. Szpilka, *Z. Phys. B* **62**, 381 (1986)

[15] A. C. Levi and E. Tosatti, *Surf. Sci.* **178**, 425 (1986);
A. Trayanov and D. Nenow, *J. Cryst. Growth* **74**, 345 (1986)

[16] A. Trayanov, A.C. Levi and E. Tosatti, to be published.

[17] J. F. van der Veen and J. W. M Frenken, *Surf. Sci.* **178**, 382 (1986)

[18] J. Q. Broughton and L. W. Woodcock, *J. Phys. C* **11**, 2743 (1978)

[19] J. Q. Broughton and G. H. Gilmer, *J. Chem. Phys.* **79**, 5095, 5105, 5119 (1983); *Acta Metall.* **31**, 845 (1983)

[20] V. Rosato ,G. Ciccotti and V. Pontikis, *Phys. Rev. B* **33**, 1860 (1986)

[21] P. Carnevali, F. Ercolessi and E. Tosatti, *Phys. Rev.*, **B36**, 6701 (1987); *Surf. Sci.* **189/190**, 645 (1987);
Phys. Rev. Lett. **59**, 2207 (1987)

[22] A. Trayanov and E. Tosatti, *Phys. Rev. B* (in Press);

[23] A. C. Levi and E. Tosatti, *Surf. Sci.* **189**, 641 (1987)

[24] R. Lipowsky, *J. Appl. Phys.* **55**, 2485 (1984)

[25] S. Dietrich, in *Phase Transitions and Critical Phenomena*, edited by C. Domb and J. Lebowitz (Academic, London, 1987), vol. 12

[26] E. Tosatti, unpublished.

[27] F. Ercolessi, *tesi di laurea*, Univ. of Trieste (1983).

[28] M. Parrinello and A. Rahman, *J. Appl. Phys.* **52**, 7182 (1981).

[29] L. Pietronero and E. Tosatti, *Sol. Stat. Comm.* **31**, 255 (1979)

[30] J. K. Kristensen and R. M. J. Cotteril, *Phil. Mag.* **36**, 437 (1977)

[31] G. F. Bolling, *Acta Metall.* **16**, 1147 (1968)

[32] J. Q. Broughton and G. H. Gilmer, *Acta Metall.* **31**, 845 (1983)

[33] M. P. Nightingale, W. F. Saam and M. Schick, *Phs. Rev. Lett.* **51**, 1275 (1983)

[34] D. E. Sulivan and M. M. Telo da Gama, in *Fluid interfacial Phenomena*, edited by C. A. Croxton, p. 45, Wiley, New York (1986)

[35] M. J. de Oliveira and R. B. Griffiths, *Surf. Sci.* **133**, 365 (1978)

[36] V. Privman, *J. Chem. Phys.* **81**, 2463 (1984)

[37] R. Lipowsky, *Z. Phys. B* **55**, 345, (1984)

[38] R. Lipowsky, *Phys. Rev. Lett.* **57**, 2876 (1986)

[39] A. Trayanov and E. Tosatti, to be published

[40] S. Nosé and F. Yonezawa, *J. Chem. Phys.*, **84**, 1803 (1985)

[41] J. W. Gibbs, *Collected works*, **Vol. 1**, Yale university press, New Haven (1928)

[42] J. Q. Broughton, A. Bonissent and F. F. Abrahm, *J. Chem. Phys.* **74**, 4029 (1981)

[43] E. Tosatti, in *The Structure of Surfaces II*, ed. by J. F. van der Veen and M. A. Van Hove (Springer, 1988), P. 535

Impurity-Impurity Interaction
in The Honeycomb Lattice

Contents

i

Introduction

It is well known [1] that in a metal, charge-charge interaction exhibits an oscillatory form and decays with distance as power-law, due to the screening effects. Precisely, the interaction potential $\phi(r)$ is given by:

$$\phi(r) = \frac{\cos(2k_F r + \eta)}{r^d},\tag{.1}$$

where k_F is the Fermi wave number, η a phase shift due to the scattering of the electrons with the impurity center, and d the space dimension. In an insulator instead, the interaction decays exponentially with distance.

Graphite is in an intermediate case, it is semi-metal. Consider a tight binding, spinless model hamiltonian for two-dimensional graphite:

$$H_0 = \frac{t}{2} \sum_{\underline{l}_A, \underline{l}_B, <\underline{l}_A, \underline{l}_B>} |\underline{l}_A> < \underline{l}_B| + |\underline{l}_B> < \underline{l}_A|,\tag{.2}$$

where $\frac{t}{2}$ ($t < 0$) is the hopping energy, and the kets $|\underline{l}>$ are tight binding orbitals centered at site $\underline{l}$. The sites form a honeycomb lattice as illustrated in fig .1, which consists of two sublattices 'A' and 'B'. The sum with the condition $<\underline{l}_A, \underline{l}_B>$ limits $\underline{l}_A$ and $\underline{l}_B$ to be nearest neighbors.

It is easy to obtain the band structure (see appendix A.1) of this simplified model hamiltonian. There are two bands touching at one point (the point P, see fig. .2). The lower band which is located between $-1.5t$ and $0t$, is a bonding band; while the upper band is an anti-bonding band, and is between $0t$ and $1.5t$. There is a saddle-point at the middle of each of the two bands, precisely at $-0.5t$ and $+0.5t$.

If we make the sublattices inequivalent by, e.g., adding a perturbative
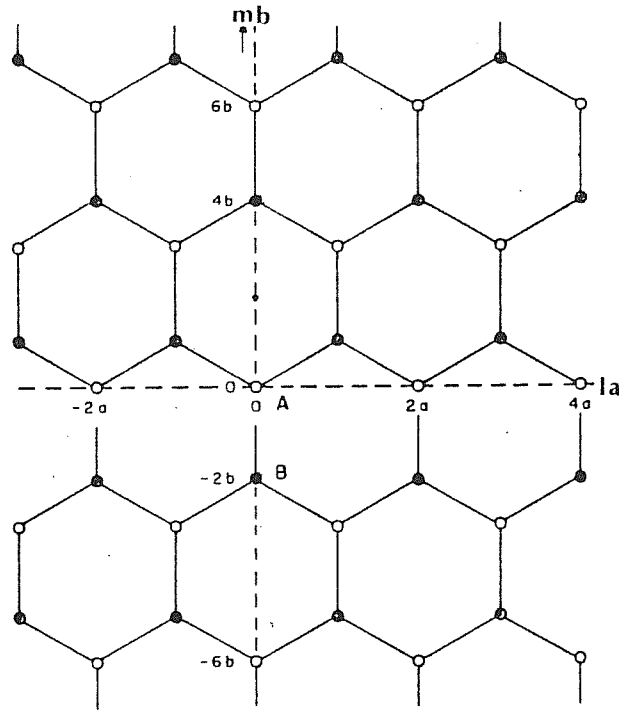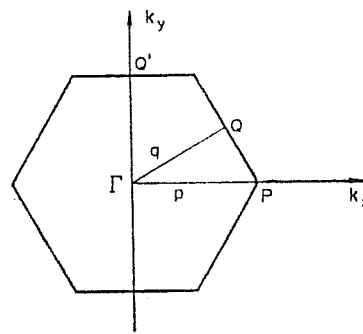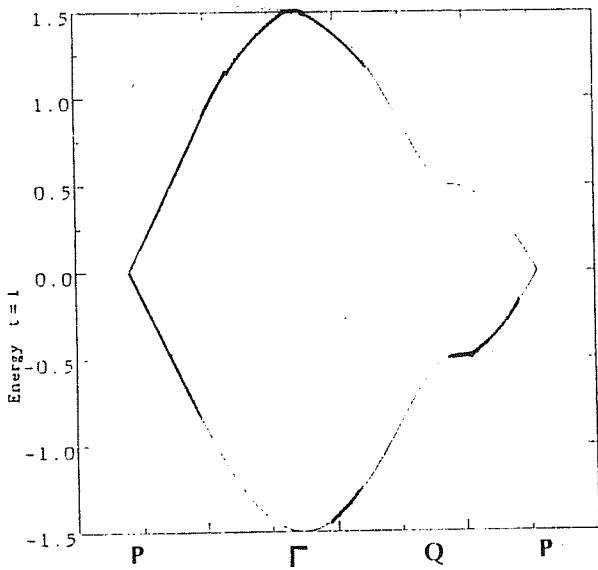
1

Figure .1:

Honeycomb lattice formed by two sublattices: 'A' (open circle) and 'B' (closed circle).

Two-dimensional Brillouin zone for graphite (or hexagonal BN).

Figure .2:

Band structure (left figure) of our model graphite hamiltonian (equation .2). The right figure shows the first Brillouin zone.
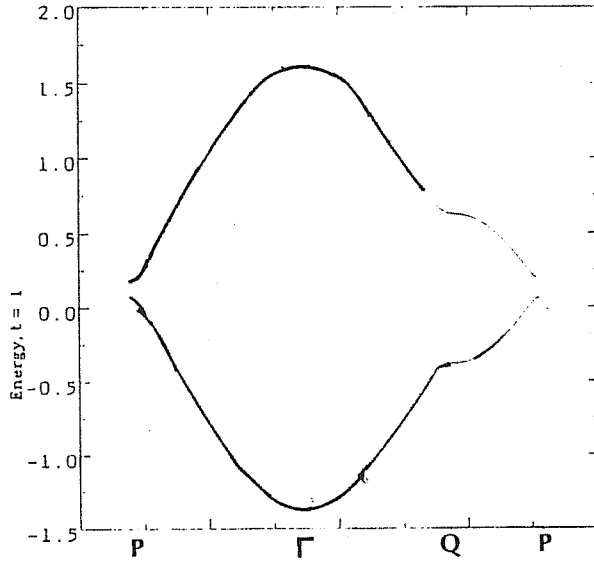
Figure .3:

Boron nitride band structure, obtained by doping one sublattice of the model graphite system, with doping amplitude $V = 0.25t$.

hamiltonian

$$H_1 = \sum_{l_B} |l_B> V_1 < l_B|, \tag{.3}$$

the zero gap in the band structure will be broken (see fig. .3). This corresponds to the well known boron nitride structure (BN).

A single impurity in 2-D graphite, $V_1|l_B >< l_B|$, though obviously unable to create a gap, will produce a disturbance around the site l_B. This disturbance can be picked up by a second impurity, giving rise to an interaction between them. In this thesis, we consider the impurity-impurity interaction in our model 2-D graphite system. The interest is many-fold:

- Find out the interaction which replaces equation .1 for 2-D semi-metal;

- Obtain an estimate for the electronic part of the lateral intercalate-intercalate interaction in graphite;

- Obtain, by straightforward analogy, the form of the hole-hole interaction in a magnetic system with two insulated "Fermi points",

3

such as the so called "s + id" *RVB* phase, postulated for the Hubbard model [2,3,4,5]. There one deals with magnetic excitations instead of charge excitations.

Starting with the very simple hamiltonian defined in Eq. .2, we dope the system by adding two point-like impurities, situated at different sites, with impurity potentials V_1 and V_2. In the thermodynamic limit, the Fermi level will not be changed by this extremely weak doping, and we look for the interaction potential between these two impurities. Our approach is as follows.

We first calculate the unperturbed Green's function with a very accurate method (see chapter 2), and then obtain the perturbed one by Dyson's equation. The impurity-impurity interaction is then obtained, by calculating the total energy change, due to the simultaneous presence of the two impurities, minus the individual energy changes caused by each impurity.

In chapter 1, we describe some theoretical preliminaries of the Green's function theory of impurity problem. We present a very efficient way of calculating the unperturbed Green's function in chapter 2. Extreme numerical accuracy is crucial in this problem, as one deals with exceedingly small differences between large numbers. Finally, we show some results obtained, together with some discussion in chapter 3. Some detail of mathematical calculations are described in the appendix.

Chapter 1

Theoretical Preliminary

To set up our theoretical bases, we review some Green's function theory of impurity problem in this chapter. For more detailed descriptions, we refer to the standard text books such as the reference [6].

The ground state energy E_0 of a system of non-interacting electrons is given by:

$$E_0 = \int_{-\infty}^{\epsilon_F} d\epsilon N_0(\epsilon)\epsilon. \tag{1.1}$$

Here $N_0(\epsilon)$ is the density of states (DOS) and can be expressed in terms of the Green's function $G_0(\epsilon)$,

$$N_0(\epsilon) = -\frac{1}{\pi} Im\{T[G_0(\epsilon)]\}, \tag{1.2}$$

where T means to take the trace, and ϵ_F is the Fermi energy, defined through the normalization of particle density $N_0(\epsilon)$:

$$\int_{-\infty}^{\epsilon_F} N_0(\epsilon)d\epsilon = \mathcal{N}, \tag{1.3}$$

where $\mathcal{N}$ is the total number of particles in the system. In our 2-D model graphite system, the Fermi level $\epsilon_F = 0$ (see Fig. .2).

The real problem of calculating the total energy, is to find out the Green's function in a convenient way. In a perfect crystal, Bloch state representation is a good candidate. We write the Green's function (as in common use, the Green's operator is also called Green's function

throughout this thesis) as

$$G_0(\epsilon) = \sum_{\underline{k}} \frac{|\underline{k})(\underline{k}|}{\epsilon - E(\underline{k}) + i\delta}, \tag{1.4}$$

where $|\underline{k})$ is the Bloch state defined in equation A.2, and $E(\underline{k})$ is the eigenvalue associated.

Doping the system, we distort the periodicity of the crystal. However, in the weak doping limit, Dyson's equation provides a straightforward way of calculating the perturbed Green's function in terms of the unperturbed ones:

$$G = G_0 + G_0 T G_0, \tag{1.5}$$

where T is the well known T matrix containing information of the scattering center.

In particular, adding one impurity with potential V_1 at site $\underline{l}$, we generate a perturbative hamiltonian

$$H_1 = |\underline{l} > V_1 < \underline{l}|. \tag{1.6}$$

The corresponding T matrix is given by:

$$
\begin{aligned}
T &= H_1 + H_1 G_0 H_1 + H_1 G_0 H_1 G_0 H_1 + \cdots \\
&= |\underline{l} > t_l(V_1) < \underline{l}| \\
t_l(V_1) &= \frac{V_1}{1 - V_1 G_0(\underline{l},\underline{l})}
\end{aligned} \tag{1.7}
$$

Upon substitution of equation 1.7 into equation 1.5, we obtain the perturbed Green's function G_1 [6]:

$$G_1 = G_0 + G_0 |\underline{l} > \frac{V_1}{1 - V_1 G_0(\underline{l},\underline{l})} < \underline{l}| G_0. \tag{1.8}$$

The change of DOS δN_1 can then be obtained through:

$$
\begin{aligned}
\delta N_1(\epsilon; \underline{l}, V_1) &= \sum_{\underline{m}} (G_1(\underline{m},\underline{m}; \epsilon) - G_0(\underline{m},\underline{m}; \epsilon)) \\
&= \sum_{\underline{m}} < \underline{l}|G_0|\underline{m} > t_l(V_1) < \underline{m}|G_0|\underline{l} > \\
&= \frac{1}{\pi} Im \frac{V_1 G_0{'}(\underline{l},\underline{l}; \epsilon)}{1 - V_1 G_0(\underline{l},\underline{l}; \epsilon)}.
\end{aligned} \tag{1.9}
$$

6

Here we have used the following fact:

$$\sum_{\underline{m}} <\underline{l}|G_0|\underline{m}><\underline{m}|G_0|\underline{l}> \quad = \quad <\underline{l}|G_0{}^2|\underline{l}>$$

$$= \quad -G_0{}'(\underline{l},\underline{l}) \qquad (1.10)$$

where $G_0{}'(\epsilon)$ is the derivative of $G_0(\epsilon)$ with respect to ϵ.

There is a discrete level E_p outside the band, given by the zero of the denominator in the right-hand side in equation 1.9,

$$G_0(\underline{l},\underline{l}; E_p) = 1/V_1 \qquad (1.11)$$

Hence, the normalization condition in equation 1.3, is equivalent to

$$\int_{\epsilon_B}^{\epsilon_F} d\epsilon \delta N_1(\epsilon) = -1, \qquad (1.12)$$

with ϵ_B the lower band edge. In the thermodynamic limit, the band edges should not be changed by doping one or two impurities. However, due to the finiteness of δ in practical calculations, which causes a spread of the sharp band edge (for details see chapter 3), ϵ_B is slightly changed (for an attractive impurity potential, ϵ_B is lowered). Equation 1.12 is then used to find out the value of ϵ_B in calculating the one impurity induced energy change δE_1, given by

$$\begin{aligned}
\delta E_1(\underline{l}, V_1) &= \int_{-\infty}^{\epsilon_F} d\epsilon \ \epsilon \delta N_1(\epsilon) \\
&= \int_{\epsilon_B}^{\epsilon_F} d\epsilon \ \epsilon \delta N_1(\epsilon) + E_p \qquad (1.13)
\end{aligned}$$

Doping the system with another impurity, e.g., at site $\underline{m}$ and with potential V_2, we add another perturbative hamiltonian:

$$H_2 = |\underline{m}> V_2 <\underline{m}|. \qquad (1.14)$$

The perturbed Green's function includes now, not only the two single impurity scattering processes, but also the two-center multiple scattering processes. It is possible to calculate the change of DOS induced by these two point-like impurities [6]. It is given by:

$$\begin{aligned}
\delta N_2(\epsilon) &= \frac{1}{\pi} Im\{[t_l G_0{}'(\underline{l},\underline{l}; \epsilon) + t_m G_0{}'(\underline{m},\underline{m}; \epsilon)] + \\
&\quad t_l(V_1)t_m(V_2)[G_0{}'(\underline{m},\underline{l}; \epsilon)G_0(\underline{l},\underline{m}; \epsilon) + \\
&\quad G_0{}'(\underline{l},\underline{m}; \epsilon)G_0(\underline{m},\underline{l}; \epsilon)]f_{ml}\}, \qquad (1.15)
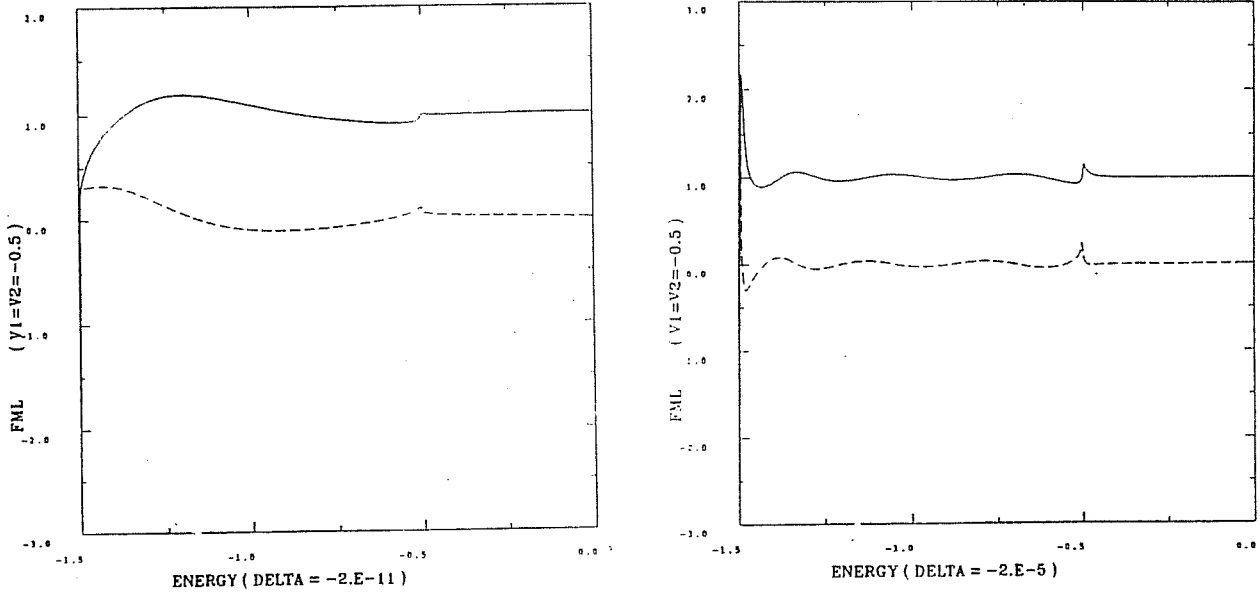\end{aligned}$$

7

Figure 1.1:

The factor f_{ml} as a function of energy. Suppose that one impurity is at the origin, then the left figure corresponds to the case where the other impurity sits at $\underline{m} = (2,0)$, while the right figure corresponds to $\underline{m} = (6,0)$.

where f_{ml} is defined as:

$$f_{ml}(\epsilon) = \frac{1}{1 - t_l t_m G_0(\underline{m}, \underline{l}; \epsilon) G_0(\underline{l}, \underline{m}; \epsilon)} \qquad (1.16)$$

The factor f_{ml} converges to one very rapidly as the distance between the two sites increases (see fig. 1.1). Based on this fact, we would expect the impurity-impurity interaction to decay also rapidly with distance.

Similar to the single impurity case, there are discrete levels, which are determined by the equation:

$$1 - V_2 G_{0l}(\underline{m}, \underline{m}; E_{p2}) = 0 \qquad (1.17)$$

where G_{0l} is the single impurity perturbed Green's function with the impurity at site $\underline{l}$, and amplitude V_1, i.e.:

$$G_{0l}(\underline{m}, \underline{m}; \epsilon) = G_0(\underline{m}, \underline{m}; \epsilon) + G_0(\underline{m}, \underline{l}; \epsilon) t_l(V_1) G_0(\underline{l}, \underline{m}; \epsilon) \qquad (1.18)$$

The energy change can be calculated by

$$\delta E_2(\underline{l}, V_1; \underline{m}, V_2) = \int_{\epsilon_D}^{\epsilon_F} d\epsilon \; \epsilon \delta N_2(\epsilon) + \sum_{p=1}^{n_t} E_{p2} \qquad (1.19)$$

8

where n_t is the total number of discrete levels. Again normalization condition (with an expression similar to the equation 1.12, but the -1 in the right-hand side is substituted by $-n_t$) is particularly useful for determining the ϵ_B in practical calculations.

The impurity-impurity interaction ϕ is then defined as the difference:

$$\phi(\underline{l}, V_1; \underline{m}, V_2) = \delta E_2(\underline{l}, V_1; \underline{m}, V_2) - \delta E_1(\underline{l}, V_1) - \delta E_1(\underline{m}, V_2). \quad (1.20)$$

Chapter 2

A feasible way to calculate the Green's function

A common approach to calculate the Green's function G_0 is the so-called "sum over the Brillouin zone" (see equation 1.4). This method however, is extremely time consuming, expecially when small value of δ is an intrinsic necessity of the problem in hand as in our case.

In fact, in a two dimension system, the DOS exhibits discontinuities at both band edges, which produce logarithmic singularities of the real part of G_0 at the band edges (see fig. 2.1). In practical numerical calculations, δ is always finite, causing a spread of the perturbed DOS at the band edges. This spread is then enhanced by the singularity of the $Re[G_0]$ due to the impurity scattering which mixes ReG_0 and ImG_0 in the perturbed Green's function. If the value of δ is not sufficiently small, the spread could be so large, such that the continuum and the discrete level are overlapped, expecially when the latter is near to a band edge (In the single impurity problem, for $V_1 = -0.2t$, $\epsilon_B - E_p = 0.000009t$). Once this happened, the precision is drastically lowered, and calculation of a small quantity, such as interaction energy between two impurities, is practically meaningless.

Hence, it is necessary to use a better method to calculate G_0, which is not time consuming for small values of δ, and is accurate — if we want to calculate the interaction potential between the impurities. Our
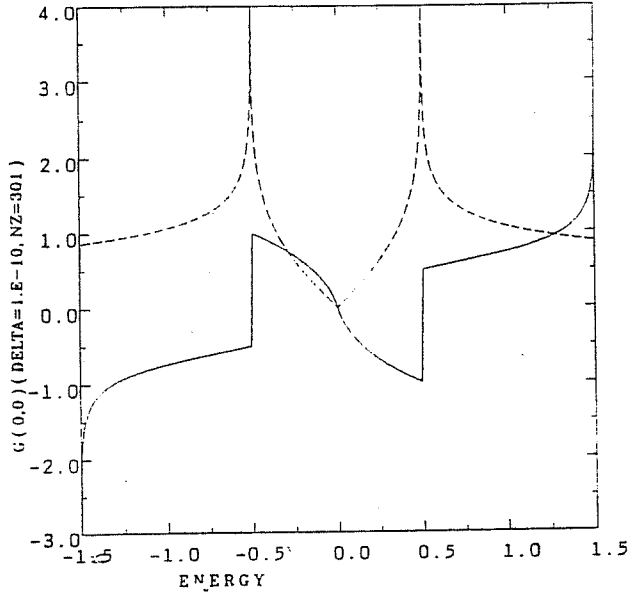
10

Figure 2.1:

Real (solid line) and imaginary (dashed line) parts of the unperturbed Green's function $G_0(0,0)$. The imaginary part is just the unperturbed DOS times π. Note that the energies are expressed in unit t.

approach is as follows:

- First, formulate the problem of calculating unperturbed Green's function as solution of the standard lattice problem [7];

- Then, map the honeycomb lattice problem into the analytically solved [7] triangular lattice problem.

- Express the triangular lattice Green's function in terms of the complete elliptic integrals of first and second kinds of complex modulus [7];

- Evaluate the complete elliptic integrals of first and second kinds by the powerful arithmetic-geometric mean method [9,8,10];

- Finally, from the unperturbed Green's function obtained through this accurate way, calculate the energy changes according to the equations in chapter 1.

11

2.1 Triangular lattice Green's function

We first introduce the triangular lattice Green's function. The analytic solution of the triangular lattice problem has been found by Horiguchi [7]. The lattice Green's function for the triangular lattice with the nearest neighbors interaction, is the solution of the following difference equation, which involves a δ-function type inhomogeneous term

$$2\epsilon_t G_t(la, mb) - G_t(la + 2a, ma) - G_t(la - 2a, mb)$$
$$-G_t(la + a, mb + b) - G_t(la + a, mb - b)$$
$$-G_t(la - a, mb + b) - G_t(la - a, mb - b)$$
$$= 2\delta_{l,0}\delta_{m,0}, \tag{2.1}$$

where $l + m$ is an even integer, and a and b are respectively equal to $\frac{1}{2}$ and $\frac{1}{2}\sqrt{3}$ times the length of the edge of the triangles.

The boundary value of the function is required to be zero as $l^2 + m^2$ tends to infinity. The solution of this equation under this boundary condition is given as follows [7]:

$$G_t(la, mb) = \frac{ab}{(2\pi)^2} \int_{-\pi/a}^{\pi/a} dx \int_{-\pi/b}^{\pi/b} dy$$
$$\times \frac{e^{i(lax + mby)}}{\epsilon_t - \cos 2ax - 2\cos ax \cos by}. \tag{2.2}$$

It is invariant under the rotation of the coordinate axes around the origin, by an angle $\frac{1}{3}(n\pi)$, $n = 1, 2, 3, 4, 5$,

$$G_t(la, mb) = G_t(la\cos\frac{1}{3}(n\pi) - mb\sin\frac{1}{3}(n\pi), la\sin\frac{1}{3}(n\pi) + mb\cos\frac{1}{3}(n\pi)), \tag{2.3}$$

and under the inversion on la axis and mb axis (cf. Fig. 2.2),

$$G_t(la, mb) = G_t(la, -mb) = G_t(-la, mb). \tag{2.4}$$

Using Eq. 2.3 for $n = 5$ and Eq. 2.4 for the inversion on mb axis, one obtains the following equation by which the function $G_t(la, mb)$ for $mb > 3la$ is expressed in terms of the one for $mb < 3la$:

$$G_t(la, mb) = G_t(\frac{1}{2}la + \frac{1}{2}\sqrt{3}mb, \frac{1}{2}\sqrt{3}la, -\frac{1}{2}mb). \tag{2.5}$$
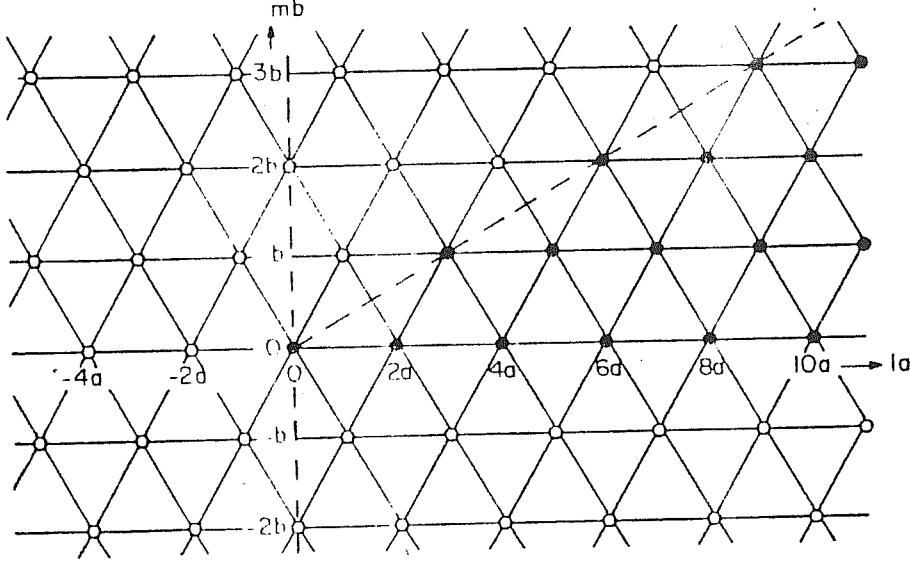
12

Figure 2.2:

The network of triangular lattice.

Thus it is sufficient to calculate only the values at lattice sites shown by the black points in Fig. 2.2.

It can be shown [4] that for any complex variable ϵ_t, the functions $G_t(0,0)$, $G_t(2,0)$ and $G_t(4,0)$ may be expressed as (From now on, for simplicity, we write $G_t(la, mb)$ as $G_t(l,m)$):

$$
\begin{aligned}
G_t(0,0) &= (1/2\pi)g\tilde{K}(k) \\
G_t(2,0) &= (\epsilon_t/6\pi)g\tilde{K}(k) - \frac{1}{3} \\
G_t(4,0) &= \frac{1}{2\pi}g(f_1(k)\tilde{K}(k) + f_2(k)\tilde{E}(k)) - f_3(k),
\end{aligned}
\tag{2.6}
$$

with

$$
\begin{aligned}
f_1(k) &= \frac{3(\alpha^2 - 2)(k^2 + \alpha^2 - 2) + (k^2 - 2\alpha^2 + \alpha^4)\epsilon_t}{3(k^2 - \alpha^2)\alpha^2} \\
f_2(k) &= \frac{4(\alpha^2 - 1)}{(k^2 - \alpha^2)\alpha^2} \\
f_3(k) &= \frac{2(k^2 - 2\alpha^2 + \alpha^4)}{3(k^2 - \alpha^2)\alpha^2} \\
g &= 8[(2\epsilon_t + 3)^{1/2} - 1]^{3/2}[(2\epsilon_t + 3)^{1/2} + 3]^{1/2}
\end{aligned}
$$

13

$$\alpha^2 = 4/\left[1 - (2\epsilon_t + 3)^{1/2}\right]^2$$

$$k = 4(2\epsilon_t + 3)^{1/4}/\left[(2\epsilon_t + 3)^{1/2} - 1\right]^{3/2}\left[(2\epsilon_t + 3)^{1/2} + 3\right]^{1/2}, \quad (2.7)$$

and $\tilde{K}(k)$ and $\tilde{E}(k)$ are given as follows:

$$\tilde{K}(k) = \begin{cases} K(k) & \text{for } \{Im\epsilon_t\}\{Imk\} < 0; \\ K^{(2)}(k) & \text{for } Im\epsilon_t > 0 \text{ and } Imk > 0; \\ K^{(3)}(k) & \text{for } Im\epsilon_t < 0 \text{ and } Imk < 0, \end{cases} \quad (2.8)$$

$$\tilde{E}(k) = \begin{cases} E(k) & \text{for } \{Im\epsilon_t\}\{Imk\} < 0; \\ E^{(2)}(k) & \text{for } Im\epsilon_t > 0 \text{ and } Imk > 0; \\ E^{(3)}(k) & \text{for } Im\epsilon_t < 0 \text{ and } Imk < 0, \end{cases} \quad (2.9)$$

where

$$\begin{aligned} K^{(2)}(k) &= K(k) + 2iK'(k) \\ E^{(2)}(k) &= E(k) + 2i[K'(k) - E'(k)] \\ K^{(3)}(k) &= K(k) - 2iK'(k) \\ E^{(3)}(k) &= E(k) - 2i[K'(k) - E'(k)]. \end{aligned} \quad (2.10)$$

Here, $K(k)$ and $E(k)$ are respectively complete elliptic integrals of the first and second kind (see Abramowitz et. al. [9]), K' and E' are the complementary quantities of K and E respectively,

$$\begin{aligned} K'(k) &= K(k') \\ E'(k) &= E(k'), \end{aligned} \quad (2.11)$$

where k' is the so-called complementary modulus of k,

$$k' = (1 - k^2)^{1/2}. \quad (2.12)$$

Recurrence formulae are particularly useful in numerical calculations. It can be shown [7] that, on the la axis, the values of $G_t(l, 0)$ at an arbitrary lattice site can be calculated through the following recurrence formula:

$$\begin{aligned} G_t(l + 4, 0) &= [1/(l + 2)][4(l + 1)(\epsilon_t + 1)G_t(l + 2, 0) \\ &\quad - 2l(2\epsilon_t^2 - 3)G_t(l, 0) + 4(l - 1)(\epsilon_t + 1) \\ &\quad \times G_t(l - 2, 0) - (l - 2)G_t(l - 4, 0)], \end{aligned}$$

$$(2.13)$$

14

where l is even. From this equation, the values of $G_t(l,0)$ for $l \geq 6$ can be calculated from the knowledge of $G_t(0,0)$, $G_t(2,0)$ and $G_t(4,0)$.

Next we consider the function $G_t(l,1)$. From Eq. 2.1, one can obtain the following equation by taking the symmetry properties 2.4 into account:

$$
\begin{aligned}
G_t(l+1,1) &= \epsilon_t G_t(l,0) - \frac{1}{2}\left[G_t(l+2,0) + G_t(l-2,0)\right] - \\
&\quad G_t(l-1,1)
\end{aligned}
\tag{2.14}
$$

where l is even and larger than or equal to 2, and

$$
G_t(1,1) = G_t(2,0).
\tag{2.15}
$$

More generally, for $G_t(l,m)$, with $l \geq 4$ and $m \geq 2$, the following recurrence formula is obtained by applying Eq. 2.1 for lattice site $(l-1, m-1)$:

$$
\begin{aligned}
G_t(l,m) &= 2\epsilon_t G_t(l-1,m-1) - G_t(l-2,m) \\
&\quad -G_t(l-3,m-1) - G_t(l+1,m-1) \\
&\quad -G_t(l,m-2) - G_t(l-2,m-2).
\end{aligned}
\tag{2.16}
$$

We note that when Eq. 2.16 is used, the function $G(l,m)$ for $m > 3l$ is expressed by the one for $m < 3l$ by using the relation 2.5:

$$
G_t(l,m) = G_t(\frac{1}{2}(l+3m), \frac{1}{2}(l-m))
\tag{2.17}
$$

2.2 Mapping the honeycomb lattice problem to triangular lattice problem

In order to map the honeycomb lattice problem into the triangular lattice one, using the translational invariance of the unperturbed system, we define the following two Green's functions, $G_H{}^{AA}$ and $G_H{}^{BA}$:

$$
G_0(\underline{l}, \underline{m}; z) = \begin{cases} G_H{}^{AA}(ia, jb; z) & \text{if } \underline{l} \text{ and } \underline{m} \text{ in the same sublattice 'A';} \\ G_H{}^{BA}(ia, jb; z) & \text{if } \underline{l} \in \text{'A' and } \underline{m} \in \text{'B',} \end{cases}
\tag{2.18}
$$

where i and j are two integers, such that in cartesian coordinates $\underline{l} - \underline{m} = (ia, jb)$, with a being half of the lattice constant, and b half of the bond length, defined in figure .1. Here we have defined a complex quantity:

$$z = \epsilon + i\delta. \tag{2.19}$$

These two Green's function satisfy two difference equations of the honeycomb lattice (see equation A.11), which can be solved analytically (see section A.2):

$$
\begin{aligned}
G_H{}^{AA}(la, mb) &= 4z\frac{ab}{4\pi^2} \int_{-\pi/a}^{\pi/a} dx \int_{-\pi/b}^{\pi/b} dy \\
&\quad \times \frac{e^{i(lax+mby)}}{4z^2 - 3 - 2\cos 2ax - 4\cos ax \cos 3by}, \\
G_H{}^{BA}(la, mb) &= \frac{ab}{4\pi^2} \int_{-\pi/a}^{\pi/a} dx \int_{-\pi/b}^{\pi/b} dy \\
&\quad \times \frac{e^{i(lax+mby)}[e^{i2bx} + e^{i(-ax-by)} + e^{i(ax-by)}]}{4z^2 - 3 - 2\cos 2ax - 4\cos ax \cos 3by}. \tag{2.20}
\end{aligned}
$$

The functions $G_H{}^{AA}(la, mb)$ and $G_H{}^{BA}(la, mb)$ are invariant under the rotation of the coordinate axes around the initial lattice site by the angles $\frac{2}{3}n\pi$, $n = 1, 2$:

$$
\begin{aligned}
G_H(la, mb) &= G_H(x_1, y_1), \\
x_1 &= la\cos(\frac{2}{3}n\pi) - mb\sin(\frac{2}{3}n\pi), \\
y_1 &= la\sin(\frac{2}{3}n\pi) + mb\cos(\frac{2}{3}n\pi), \tag{2.21}
\end{aligned}
$$

and under the inversion on the vertical axis

$$G_H(la, mb) = G_H(-la, mb). \tag{2.22}$$

As we put $z = \epsilon + i\delta$, where ϵ is a real and δ a positive infinitesimal number, we can easily prove that the real and imaginary parts of $G_H{}^{AA}(z : la, mb)$ are odd and even functions respectively, and the real and imaginary part of $G_H{}^{BA}(z : la, mb)$ are even and odd functions respectively:

$$
\begin{aligned}
ReG_H(\epsilon - i\delta; la, mb) &= -\triangle_{lm}ReG_H(-\epsilon, -i\delta; la, mb) \\
ImG_H(\epsilon - i\delta; la, mb) &= \triangle_{lm}ImG_H(-\epsilon - i\delta; la, mb) \tag{2.23}
\end{aligned}
$$

16

where $\triangle_{lm}$ is plus or minus one according to whether the sites l and m belong to the same sublattice or to different sublattices.

After the parameters a and b are deleted by variable transformation, these functions $G_H{}^{AA}(la, mb)$ and $G_H{}^{AB}(la, mb)$ are expressed in terms of the lattice Green's function for the triangular lattice [7] (for simplicity, we ignore the two constants a and b in the arguments of G),

$$
\begin{aligned}
G_H{}^{AA}(l, m) &= 2zG_t(\epsilon_t; l, \frac{1}{3}m) \\
G_H{}^{BA}(l, m) &= G_t(\epsilon_t; l, \frac{1}{3}(m+2)) + G_t(\epsilon_t; l-1, \frac{1}{3}(m-1)) \\
&\quad + G_t(\epsilon_t; l+1, \frac{1}{3}(m-1)) \\
\epsilon_t &= (4z^2 - 3)/2,
\end{aligned}
\tag{2.24}
$$

where $G_t(\epsilon_t; l, m)$ is defined by equation 2.2. Thus, the analytic properties and the values of the lattice Green's function for the honeycomb lattice can be obtained from the knowledge of that for the triangular lattice.

2.3 Evaluation of the complete elliptic integrals

One of the powerful method to calculate numerically the complete elliptic integrals is the so called "arithmetic-geometric mean method" (AGM) [9,10,8]. Briefly, the method works in the following way [9] (Here we present a standard description of the AGM. For the case of complex modulus K_0 however, a modified method as described in the appendix, in section A.3, should be used.): to calculate the complete elliptic integrals at modulus k_0, one starts from a given number triple (a_0, b_0, c_0), with

$$
\begin{aligned}
a_0 &= 1 \\
b_0 &= (1 - k_0{}^2)^{1/2} \\
c_0 &= k_0,
\end{aligned}
\tag{2.25}
$$

17

and proceeds in recurrence to number triples $(a_1, b_1, c_1) \cdots (a_n, b_n, c_n)$, according to the following arithmetic geometric means:

$$a_n = (a_{n-1} + b_{n-1})/2$$
$$b_n = (a_{n-1}b_{n-1})^{1/2}$$
$$c_n = (a_{n-1} - b_{n-1})/2 \qquad (2.26)$$

and stops at i-th step when $c_i = 0$ to the degree of accuracy. Then it can be shown [9] that the complete elliptic integrals satisfy:

$$K(k_0) = \pi/(2a_i)$$
$$\frac{K - E}{K} = \frac{1}{2}(c_0{}^2 + 2c_1{}^2 + \cdots + 2c_i{}^2) \qquad (2.27)$$

This is a powerful algorithm — for a precision of 10^{-15}, it takes less than 12 iterations.

2.4   Calculation of the Green's function

Starting from calculating the complete elliptic integrals of the first and second kinds, by using the arithmetic geometric mean method, and thus calculating the modified ones $\bar{K}$ and $\bar{E}$, we can obtain the triangular lattice Green's function (see section 2.1). As an example, we show in fig. 2.3 the $G_t(0,0)$, which reproduces the singularities with high precision.

The honeycomb lattice Green's function G_H (or equivalently the G_0) can be calculated in a straight forward way with equation 2.24. In fig. 2.4 we present $G_H^{AA}(14, 0)$. Note the figure reproduces accurately the oscillations as well as the singularities.
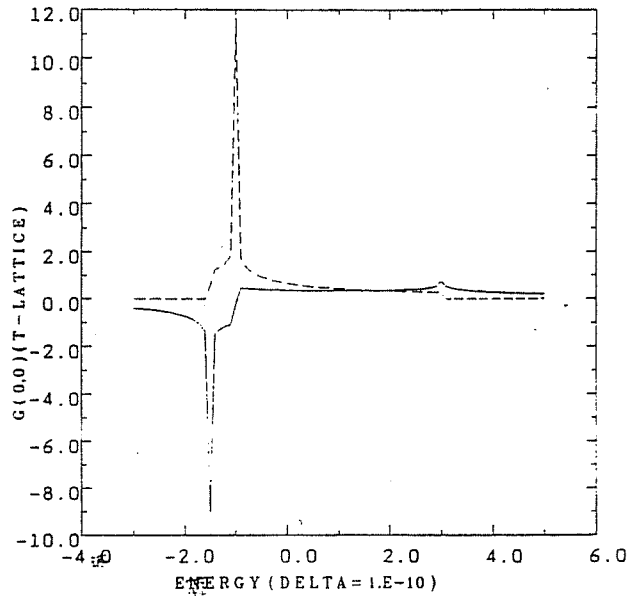
18

Figure 2.3:

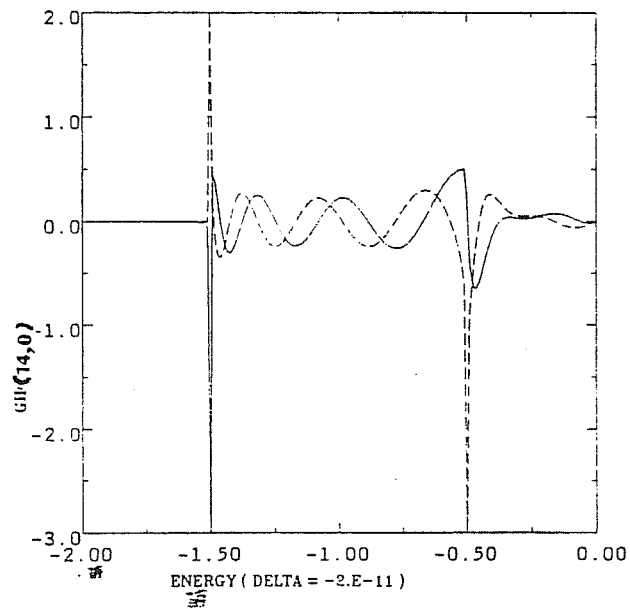The triangular lattice Green's function $G_t(0,0)$ ($\delta = -10^{-10}$). Energies are expressed in unit ϵ_t.

Figure 2.4:

Honeycomb lattice Green's function $G_H(14,0)$. Energies are expressed in unit t.

19

Chapter 3

Results and Discussion

3.1 One-impurity perturbation energy

To find the energy change induced by the single impurity perturbation, we should first find out the discrete levels, by looking for the solution of the equation

$$1 - V_1 G_0(\underline{l}, \underline{l}; z) = 0. \tag{3.1}$$

The algorithm we used is a combination of the Newton-Raphson and the bisection algorithms [11]. This algorithm has both the rapidity of the Newton-Raphson zero searching, and the safety of the bisection algorithm. Figure 3.1 shows the discrete levels as a function of the impurity potential V_1. Near the band edges, the pole E_p depends on V_1 exponentially as we expect, due to the logarithmic divergence of the DOS at the band edges. For small value of $|V_1|$, the discrete level E_p can be found only if δ is small. Typically, for $V_1 = -0.2t$, we have found that $\delta < 10^{-8}$ is necessary.

The perturbation energy is then calculated through the equation 1.13, where the change of density of states δN_1 is calculated by using equation 1.9. In calculating δN_1, the derivative of the Green's function is obtained by calculating the derivatives of the complete elliptic integrals, through the following analytic relation [9]:

$$\frac{dK(k)}{dk} = \frac{1}{k'^2} \left\{ \frac{E(k) - k'^2 K(k)}{k} \right\}$$
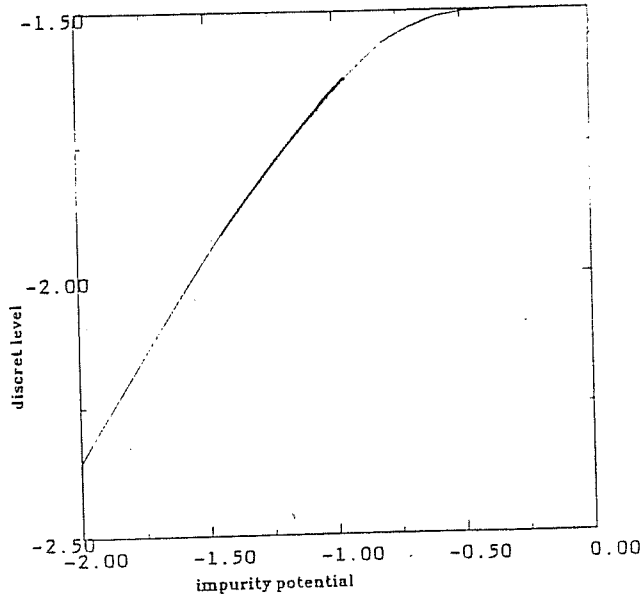
Figure 3.1:

Discrete levels as function of the impurity potential. Energies are expressed in unit t. The curve is specular ($E_p(-V) = -E_p(V)$) for a repulsive perturbation V.

$$\frac{dE(k)}{dk} = \frac{E(k) - K(k)}{k} \qquad (3.2)$$

The calculation of the integrals is quite hard, due to the bad behavior of the integrand. In fact, the main contributions to δE_1 come from the lower band edge (for attractive potential) and the saddle point, where the δN_1 exhibits singularities (see figure 3.2). We have found the 5-th order adaptive Runge-Kutta algorithm [11] most appropriate. This algorithm was originally used for solving differential equations. It is not difficult, however, to use it also for integration, because the derivative of the primitive function equals the integrand.

Generally, the lower integral bound ϵ_B is slightly lower than $-1.5t$ (for attractive potential), as the impurity caused spread of the band edge. In practice, the value of ϵ_B is varied as varying V_1, and is de-termined by the normalization condition (see equation 1.12). We have calculated δE_1 for V_1 varying form $-0.2t$ to $-2t$ (see table 3.1 and figure 3.3). High precision of the integration is necessary to have mean-ingful results. As a test of convergence, we have varied δ from 10^{-8}
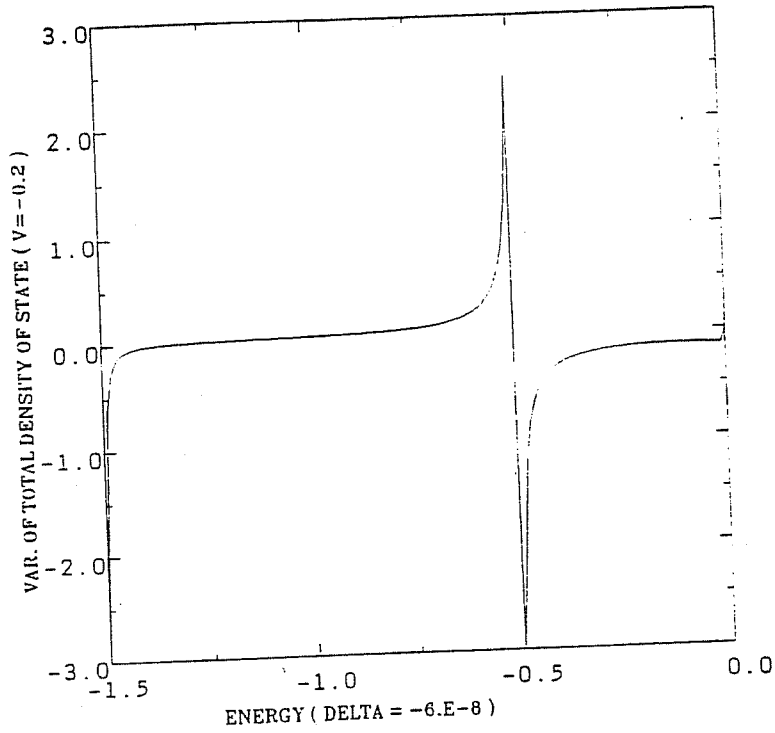
21

Figure 3.2:

Single impurity induced change of density of states. Note that the energies are expressed in unit t.

to 10^{-11}, obtaining the same results within the fourth decimal number, provided the normalization is optimized.

It is known that the unperturbed density of states $\rho_0(\underline{l}; \epsilon)$ exhibits a discontinuity as ϵ approaches the band edge [6], i.e.,

$$\rho_0(\underline{l}; \epsilon) \xrightarrow{\epsilon \to \epsilon_B^+} \rho_d. \tag{3.3}$$

As a result

$$G_0(\underline{l}, \underline{l}; \epsilon) \xrightarrow{\epsilon \to \epsilon_B^-} \rho_d \ln |(\epsilon - \epsilon_B)/C|, \tag{3.4}$$

where C is a positive constant. Thus for very small $|V_1|$, E_p lies very close to the band edge and one can use equation 3.4 for $G_0(\underline{l}, \underline{l}; \epsilon)$. Substituting equation 3.4 into 1.11 we obtain

$$E_p \overset{V_1 \leq 0}{\simeq} \epsilon_B - C \exp\left(-\frac{1}{|V_1|\rho_d}\right). \tag{3.5}$$

On the other hand, the continuum integral in the equation 1.13 depends on V_1 linearly, for $|V_1| \to 0$ (see equation 1.9). We can thus conclude that in the small $|V_1|$ limit, the energy change induced by the single impurity perturbation depends linearly on the impurity potential V_1. Figure 3.3 confirms this expectation.

22

V_1	E_p	ϵ_B	$Normalization$	δE_1
−0.2	−1.500009	−1.50000005	−0.9995114	−0.1080
−0.3	−1.500033	−1.50000008	−1.0000060	−0.1661
−0.4	−1.500690	−1.50001000	−1.0000236	−0.2283
−0.5	−1.504205	−1.50001000	−1.0000249	−0.2938
−0.6	−1.513908	−1.50001000	−1.0000199	−0.3623
−0.7	−1.532382	−1.50000010	−1.0000068	−0.4335
−0.8	−1.560581	−1.50000005	−0.9999995	−0.5074
−1.0	−1.644042	−1.50000005	−0.9999994	−0.6619
−1.2	−1.756088	−1.50000005	−1.0000081	−0.8241
−1.3	−1.820115	−1.50000005	−0.9999998	−0.9076
−1.4	−1.888337	−1.50000005	−0.9999963	−0.9925
−1.5	−1.960087	−1.50000003	−0.9999937	−1.0787
−1.6	−2.034827	−1.50000003	−0.9999948	−1.1166
−1.7	−2.112116	−1.50000003	−0.9999916	−1.2544
−1.8	−2.191594	−1.50000003	−0.9999912	−1.3436
−1.9	−2.272964	−1.50000003	−0.9999932	−1.4337
−2.0	−2.355982	−1.50000003	−0.9999935	−1.5245

Table 3.1:

Results of one impurity perturbation problem ($\delta = 4.\ 10^{-11}$ is used). The upper bound E_F of the integral is kept to be zero. Adjusting the lower bound ϵ_B to optimize the normalization, we obtained the same results of δE_1 up to the fourth decimal number, for δ varying from 10^{-8} to 10^{-11}. Note that the energies are expressed in unit t.
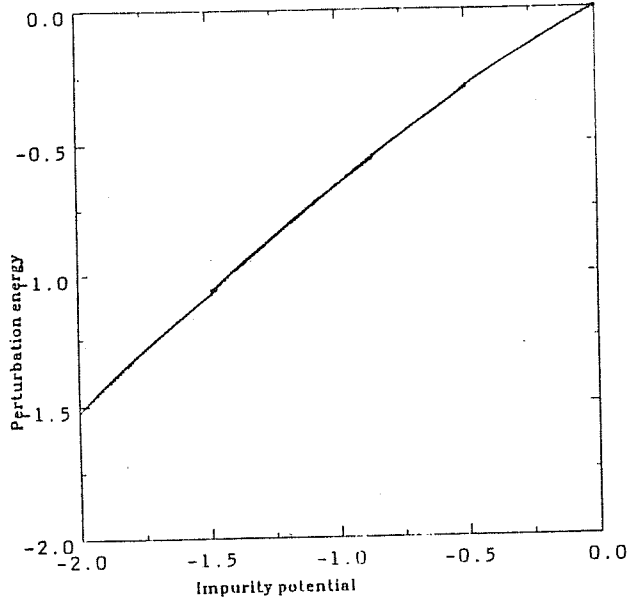
Figure 3.3:

One impurity perturbation energy as function of impurity potential. The energy tends linearly to zero as is expected (see the text). Note that the energies are expressed in unit t.

3.2 Impurity-impurity interaction

The calculation of δE_2 is similar to what we have done in the previous section. First, we find out the discrete levels by solving the equation 1.17. The two impurities perturbed energy δE_2 is then calculated through the equation 1.19. Finally, the interaction energy is simply the difference defined in equation 1.20. In table 3.2 we present results for the case where $V_1 = -0.5t$, $V_2 = -0.5t$. The results for $V_1 = -0.5t$ and $V_2 = -0.7t$, are presented in table 3.3. What are written in the first column of the tables 3.2 and 3.3 are the positions of the second impurity $\underline{m}$. The other impurity is assumed at $\underline{l} = (0,0)$. Note that the interaction is repulsive when the two impurities are in the same sublattice, and attractive when they are in different sublattices. The interaction energy is smaller than the numerical error, when the distance between the two impurities is larger than $4a$ (see Fig. 3.4).

24

m	δ	ϵ_B	$Normal.$	E_p	$int.\ ene.$
(2,0)	$-4\ 10^{-11}$	-1.5008	-1.0000229	-1.52821	
	$-4\ 10^{-8}$	-1.5029	-0.9999991		-0.00115
(4,0)	$-4\ 10^{-8}$	-1.5029	-0.9999988	-1.51543	-0.00001
(6,0)	$-4\ 10^{-8}$	-1.5029	-1.0000067		
	$-8\ 10^{-8}$	-1.5035	-0.9999996	-1.51110	-0.00009
(1,1)	$-4\ 10^{-8}$	-1.5020	-0.9999985		
		-1.5028	-1.0000010	-1.54878	0.01571
(2,-2)	$-4\ 10^{-8}$	-1.5028	-0.9999924		
		-1.5030	-0.9999964	-1.52378	0.00605

Table 3.2:

Results of two impurities perturbation problem, $V_1 = -0.5t$, $V_2 = -0.5t$. Note that the energies are expressed in unit t.

m	δ	ϵ_B	$Normal.$	E_p	$int.\ ene.$
(2,0)	$-4\ 10^{-8}$	-1.5029	-0.9999991	-1.56039	-0.00144
(4,0)	$-4\ 10^{-8}$	-1.5029	-0.9999992	-1.53988	-0.00004
(6,0)	$-8\ 10^{-8}$	-1.5035	-1.0000102	-1.53463	-0.00012
(1,1)	$-4\ 10^{-8}$	-1.5028	-1.0000002	-1.59573	0.01992
(2,-2)	$-4\ 10^{-8}$	-1.5030	-0.9999951	-1.55278	0.00782

Table 3.3:

Results of two impurities perturbation problem, $V_1 = -0.5t$ and $V_2 = -0.7t$. Note that the energies are expressed in unit t.
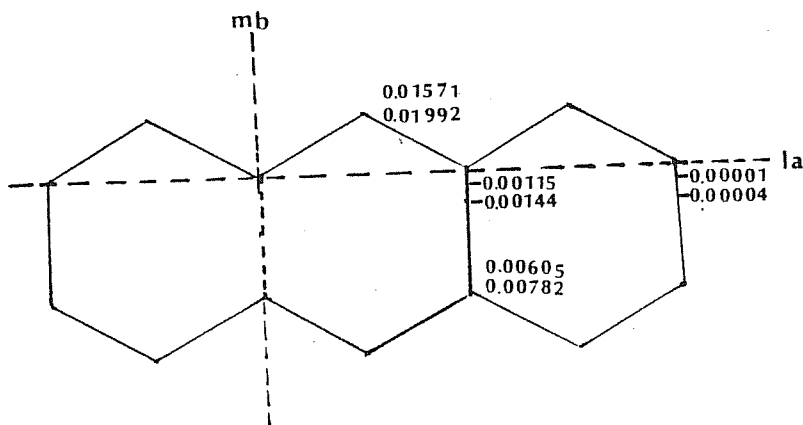
Figure 3.4:

Impurity-impurity interaction potential, with one impurity located at the origin, and the another impurity at the site where the corresponding interaction energy are written. Each site is characterized by two numbers, the upper one refers to the case $V_1 = -0.5t, V_2 = -0.5t$, and the lower one to the case $V_1 = -0.5t$, $V_2 = -0.7t$. Note that the energies are expressed in unit t. The interaction potential is repulsive for two impurities sitting at the same sublattice, and attractive otherwise.

3.3 Discussion

We have carried out calculations of the charge-charge interaction in one model graphite system (see equation .2). We have first mapped the honeycomb lattice to the triangular lattice — its dual lattice [7]. Using the results obtained by Horiguchi [7], the triangular lattice Green's function is calculated in terms of the modified complete elliptic integrals of complex modulus, which in turn are numerically calculated in an accurate way by a powerful "arithmetic geometric mean" method.

It turns out that the impurity-impurity interactions are: a) very weak, b) oscillatory, c) decaying rapidly with distance.

A crude explanation of these behaviors could be as follows:

- The weakness of the impurity-impurity interaction is very likely to result from the fact that most states in 2-D graphite are well removed from E_F. Only a tiny minority of states is near E_F, while a large pileup occurs at the saddle points, $E \simeq \pm 0.5t$ (see figure 3.2).

- The minority of states near E_F is however responsible for the long tail of the interaction potential $\phi(\underline{l}, V_1; \underline{m}, V_2)$. Since the Fermi level lies at the P-point, i.e. away from $k = 0$ and is two-fold degenerate, one can expect oscillations (analogous to the Friedel oscillation $\cos(2\vec{k}_F \cdot \vec{r})$)) like $\cos(\vec{Q} \cdot \vec{r})$, with $\vec{Q} = \vec{k}_{\Gamma P} + \vec{k}_{PQ} + \vec{k}_{Q\Gamma}$ (see figure .2).

- At the analytic level, in $d = 2$, and with a zero-gap, one could expect [1] a decay of the interaction potential like $\cos(\vec{Q} \cdot \vec{r})/r^{d+\alpha}$, with $\alpha = 1$. The present numerical results are well compatible

---

[1] The asymptotic behavior of the interaction potential ϕ can be obtained in the following way: Since the states near E_F are responsible for the long tail behavior of the interaction potential, using the well known kp approximation, we approximate the band structure as $E(\vec{k}) = -p_0 k$. It is then possible to prove that the off-diagonal unperturbed Green's function decays with distance as power law $1/r^{\frac{3}{2}}$. As ϕ is proportional to $G_0^2(\vec{l}, \vec{m})$ to leading order (see equations 1.9, 1.15, 1.16 and 1.19), we obtain for the interaction potential $\phi(r) \propto 1/r^3$.

with these analytic behaviors, but do not extend enough to provide a quantitative evaluation of α.

- To the extent to which these results can be carried over to describe the magnetic excitations of the so-called "s + i d" RVB state of the Hubbard model [2], as discussed in the introduction, it is interesting to note that they will imply attraction for holes sitting on different sublattices, and repulsion when on the same sublattice.

Appendix A

Some Detail of Calculations

A.1 Band structure

Giving the model tight binding hamiltonian defined in equation .2, we are now going to solve the following Schrödinger equation:

$$H|\underline{k}) = E(\underline{k})|\underline{k}), \tag{A.1}$$

with the Bloch state $|\underline{k})$ being linear combinations of tight binding orbitals:

$$|\underline{k}) = \sum_{l_A} \alpha(\underline{k})e^{i\underline{k}l_A}|l_A> + \sum_{l_B} \beta(\underline{k})e^{i\underline{k}l_B}|l_B> . \tag{A.2}$$

Upon substitution of equation A.2 into equation A.1, and using the ortho-normality of the orbitals, we find the following results:

$$|\alpha(\underline{k})|^2 = |\beta(\underline{k})|^2 = 1; \tag{A.3}$$

$$E(\underline{k}) = \pm|S_1(\underline{k})|; \tag{A.4}$$

$$S_1(\underline{k}) = \sum_{l_B} e^{i\underline{k}(l_A - l_B)}, \tag{A.5}$$

where the sum in equation A.5 runs over the three neighbors (see figure .1) of the site l_A.

There are two primitive lattice vectors in the graphite lattice:

$$\begin{aligned}
\underline{\tau_1} &= 2a(1/2, \sqrt{3}/2), \\
\underline{\tau_2} &= 2a(-1/2, \sqrt{3}/2),
\end{aligned} \tag{A.6}$$

29

and two reciprocal vectors:

$$\underline{h_1} = \frac{\pi}{a}(1, 1/\sqrt{3}),$$

$$\underline{h_2} = \frac{\pi}{a}(-1, 1/\sqrt{3}). \qquad (A.7)$$

Here the parameter a is half of the lattice constant. Carrying out explicitly calculation of equation A.5, we find

$$E(\underline{k}) = \pm\frac{t}{2}\sqrt{3 + 2\{\cos(k_1 - k_2)2\pi + \cos(k_1 2\pi) + \cos(k_2 2\pi)\}} \qquad (A.8)$$

with $\underline{k} = k_1\underline{h_1} + k_2\underline{h_2}$.

A.2 Difference equations of the honeycomb lattice Green's function

There are two kinds of matrix elements of the Greens' operator G_0. One $(G_0{}^{AA})$ is associated to the case where the two sites $\underline{l}$ and $\underline{m}$ are in the same sublattice 'A':

$$G_0{}^{AA}(\underline{l}, \underline{m}; \epsilon) = \sum_{\underline{k}} \frac{e^{i\underline{k}(\underline{m}-\underline{l})}}{\epsilon - E(\underline{k}) + i\delta}; \qquad (A.9)$$

the other one $(G_0{}^{BA})$ is associated to the case where the two sites are in sublattices 'B' and 'A' respectively:

$$G_0{}^{BA}(\underline{l_A}, \underline{m_B}; \epsilon) = \sum_{\underline{k}} \frac{e^{i\underline{k}(\underline{m_B}-\underline{l_A})}}{\epsilon - E(\underline{k}) + i\delta} \frac{S_1(\underline{k})}{|S_1(\underline{k})|}. \qquad (A.10)$$

Here, the sums run over the first Brillouin zone, and the function $S_1(\underline{k})$ is defined in equation A.5. Note that in equation A.9 and A.10, we have implicitly defined the superscript of G.

Using the translational invariance of the unperturbed system, we introduce the two lattice Green's functions $G_H{}^{AA}$ and $G_H{}^{BA}$, defined in the equation 2.18. Hence, upon direct substitutions of equations A.9 and A.10, and using the equations A.4, A.3, A.5, we obtain the following

two difference equations:

$$2zG_H{}^{AA}(i,j) - G_H{}^{BA}(i-1,j+1) - G_H{}^{BA}(i+1,j+1)$$
$$-G_H{}^{BA}(i,j-2) \; = \; 2\delta_{i,0}\delta_{j,0};$$

$$2zG_H{}^{BA}(i,j) - G_H{}^{AA}(i+1,j-1) - G_H{}^{AA}(i-1,j-1)$$
$$-G_H{}^{AA}(i,j+2) \; = \; 0. \quad \text{(A.11)}$$

With the boundary condition that $G_H(i,j)$ vanishes when r goes to infinite, these two equations can be solved analytically [7], i.e.:

$$G_H{}^{AA}(i,j;z) \; = \; 4z\frac{ab}{4\pi^2}\int_{-\pi/a}^{\pi/a}dx\int_{-\pi/b}^{\pi/b}dy$$
$$\frac{e^{i(lax+mby)}}{4z^2 - 3 - 2\cos 2ax - 4\cos ax \cos 3by}$$

$$G_H{}^{BA}(i,j;z) \; = \; \frac{ab}{4\pi^2}\int_{-\pi/a}^{\pi/a}dx\int_{-\pi/b}^{\pi/b}dy$$
$$\frac{e^{i(lax+mby)}[e^{i2bx} + e^{i(-ax-by)} + e^{i(ax-by)}]}{4z^2 - 3 - 2\cos 2ax - 4\cos ax \cos 3by} \quad \text{(A.12)}$$

A.3 Arithmetic geometric mean method

The complete elliptic integral of the first kind is defined as

$$K(k_0) = \int_0^{\pi/2}d\theta\frac{1}{\sqrt{1 - k_0{}^2\sin^2\theta}}, \qquad \text{(A.13)}$$

while the second kind is defined as

$$E(k_0) = \int_0^{\pi/2}d\theta\sqrt{1 - k_0{}^2\sin^2\theta}. \qquad \text{(A.14)}$$

Here the parameter k_0 is called modulus. Arithmetic geometric mean (AGM) method has been proved to be very useful in calculating the complete elliptic integrals [9]. For complex k_0, a modified AGM method has been proposed by Morita et. al. [8]. The modified AGM method consists of recursive calculations of a three number series (s_n, t_n, c_n), according to the following recurrence form:

$$a_n \; = \; 2/(1 + k'_{n-1})$$

$$k'_n = {k'_{n-1}}^{1/2} a_n$$

$$t_n = (t_{n-1} + k'_{n-1} s_{n-1}) {a_n}^2 / 2$$

$$s_n = (s_{n-1} + t_{n-1}) a_n / 2$$

$$c_n = c_{n-1} a_n \tag{A.15}$$

starting by $s_0 = 1$, $t_0 = {k'_0}^2$, and $c_0 = 1$, where $k'_0 = (1 - {k_0}^2)^{\frac{1}{2}}$. The recurrence proceeds until $k'_n = 1$ to the precision required. It can be shown [8] that $K(k_0) = \pi/(2c_n)$ and $E(k_0) = \pi/(2s_n)$.

Bibliography

[1] N. F. Mott, *"Metal-insulator Transitions"*, p. 21, Taylor & Francis ltd.

[2] G. Baskaran and P. W. Anderson, *Phys. Rev. Lett.* (1987)

[3] G. Kotliar, *Phys. Rev. B* **37**, 3664 (1988)

[4] I. Affleck and J. B. Martson, *Phys. Rev. B* **37**, 3774 (1988)

[5] D. P. Arovas and A. Auerbach, *Phys. Rev. B* **38** 316 (1988)

[6] E. N. Economu, *"Green's Function in Quantum Physics"*, Springer series in solid state science, **Vol. 7**, (1983)

[7] T. Horiguchi, *J. Math. Phys.* **13**, 1411 (1972)

[8] T. Morita and T. Horiguchi, *Numer. Math.* **20**, 425 (1973)

[9] M. Abramowitz and I. M. Stegun, *"Hand Book of Mathematical Functions with Formulars, Graphs, and Math. Tables"*, New York, Dover pub. Inc. (1965)

[10] R. Burlisch, *Numer. math.* **7**, 78 (1965)

[11] W. H. Press, B. P. Flannery, S. B. Tenholsky and W. T. Vetterling, *"Numerical recipies"*, Cambridge univ. press. (1987).

Acknowledgements